J. Fluid Mech. (2001), *vol.* 426, *pp.* 1–45. Printed in the United Kingdom

Direct numerical simulations of the Crow instability and subsequent vortex reconnection in a stratified fluid

By J. F. GARTEN[1,2]†, J. WERNE[1],
D. C. FRITTS[1,2] AND S. ARENDT[1]

[1]Colorado Research Associates, 3380 Mitchell Lane, Boulder, CO 80301, USA

[2]Program in Atmospheric and Oceanic Sciences, University of Colorado, Boulder, CO 80309-0311, USA

(Received 21 December 1998 and in revised form 19 June 2000)

The evolution of a vertically propagating three-dimensional vortex pair in ambient stratification is studied with a three-dimensional numerical model. We consider a range of Reynolds (*Re*) and Froude (*Fr*) numbers, and initialize the vortex pair in a configuration that promotes growth of the Crow instability (Crow 1970). The growth rate of the instability is *Re* dependent, and we present a method for extending Crow's model to predict this dependence. We also find that relatively strong ambient stratification ($Fr \leqslant 2$) further alters the growth of the instability via advection by baroclinically produced vorticity. For all of our cases with $Fr \geqslant 1$ (including our unstratified cases where $Fr \rightarrow \infty$), the instability leads to vortex reconnection and formation of a vortex ring. A larger *Re* delays the commencement of the reconnection, but it proceeds more rapidly once it does commence. We compute a reconnection time scale (t_R), and find that $t_R \sim 1/Re$, in agreement with a model formulated by Shelley *et al.* (1993). We also discuss a deformative/diffusive effect (related to yet distinct from the curvature reversal effect discussed by Melander & Hussain 1989) which prevents complete reconnection. Ambient stratification (in the range $Fr \geqslant 1$) accelerates the reconnection and reduces t_R by an amount roughly proportional to $1/Fr$. For some *Fr*, stratification effects overwhelm the deformative effect, and complete reconnection results.

1. Introduction

We discuss the results of direct numerical simulations of three-dimensional anti-parallel vortex pairs evolving in ambient stratification. The study of anti-parallel vortex pairs evolving under a variety of environmental conditions has general relevance to the study of aircraft trailing vortices, which can pose considerable hazard to other aircraft (Olsen, Goldburg & Rogers 1971). Spalart (1998) has recently presented an excellent survey of this field that highlights the major controversies. Although our restricted Reynolds number (*Re*) range prevents direct application of our results to the pressing issues regarding real-world ATC methods, we note that three-dimensional vortex pairs are also found within convective instabilities, such as those occurring

---

† Current address: Space Physics Research Laboratory, 2455 Hayward St., University of Michigan, Ann Arbor, MI 48109, USA.

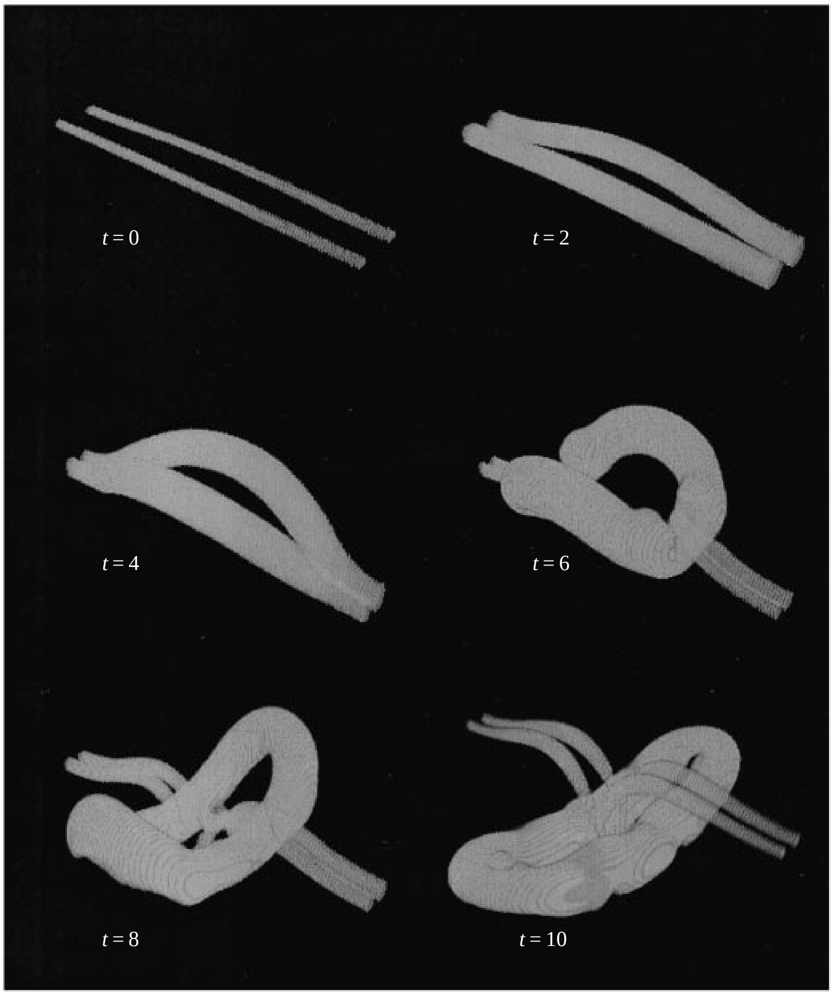

FIGURE 1. Volume renderings of λ_2 viewed from above showing large negative values of λ_2 at the times shown for the unstratified case with $Re = 942$.

in a breaking gravity wave (Andreassen *et al.* 1994) and fully-developed turbulence (Rogers & Moin 1987), to name two examples.

Our purpose here is to investigate how stratification affects the evolution of anti-parallel vortices, from their initial evolution dominated by the growth of the Crow instability, to their reconnection and rearrangement into vortex rings. Overviews of two of our simulations are shown in figures 1 (the unstratified case with $Re = 942$) and 2 (the case with $Re = 942$ and $Fr = 2$, where Froude number Fr is defined in § 2.2); although the flow evolves continuously in time, we will separately discuss the different mechanisms that control the flow during different stages of the evolution. For our solutions, the Crow instability is the dominant mechanism from the initialization of the flow to about $t \simeq 3.5$–4, while the subsequent vortex reconnection is the dominant mechanism from roughly that time to $t \simeq 6$–8 (these time scales depend on Re and Fr; see figures 1 and 2, and 7 and 11). As much previous work exists on both the Crow instability and the general topic of vortex reconnection, we now include introductory material for both.

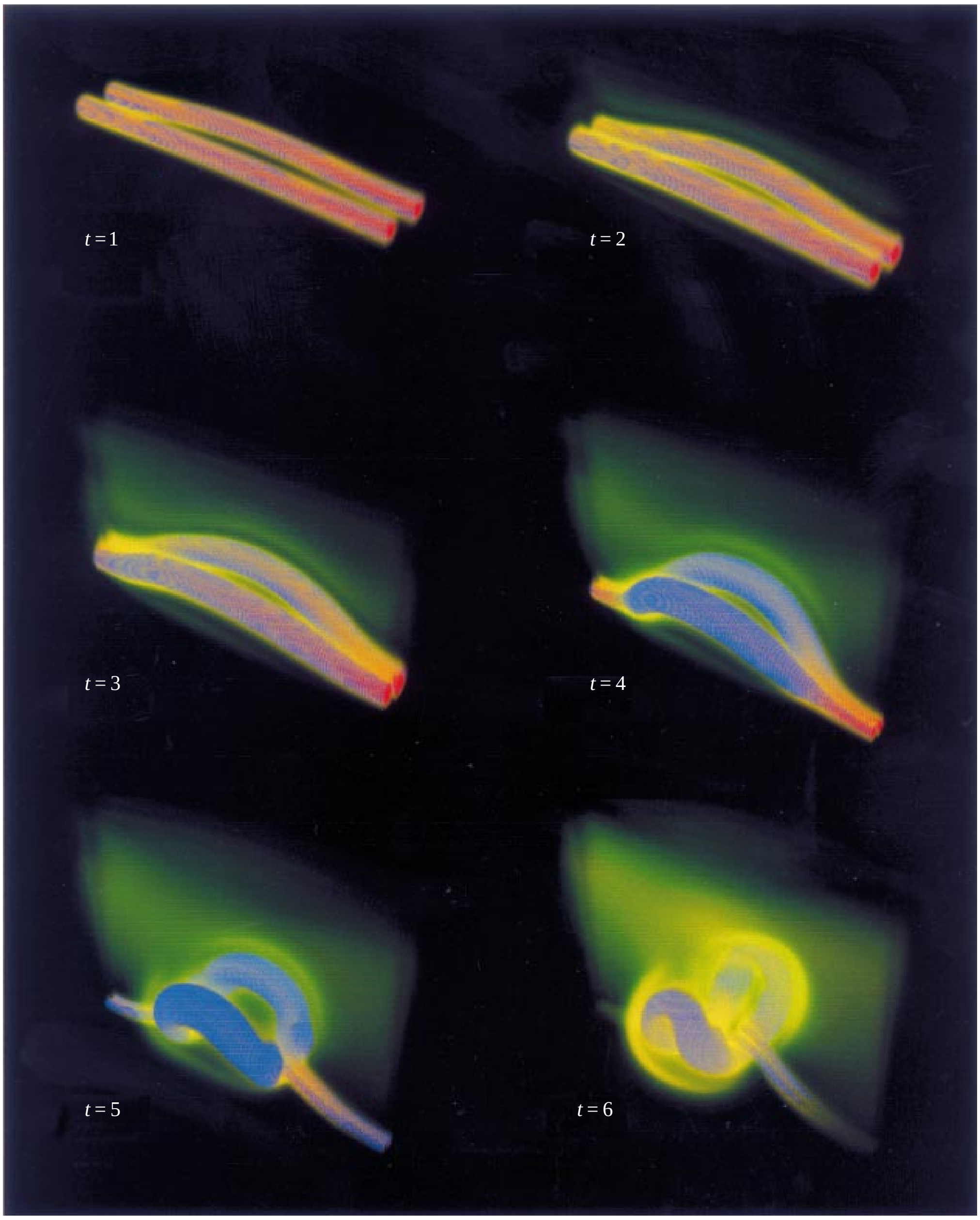

FIGURE 2. Volume renderings of both λ_2 and $|\omega|$ viewed from above at the times shown for the case with $Re = 942$ and $Fr = 2$. The colour and opacity scales are such that large negative values of λ_2 are blue and opaque, while large values of $|\omega|$ are red and opaque, and small values of $|\omega|$ are green and transparent. The green cloud of vorticity outside the primary vortices stems from baroclinic production (see §4.2 and figure 13).

Using a linear perturbation analysis of anti-parallel vortex tubes (with constant cross-section) in an unstratified, incompressible, and inviscid fluid, Crow (1970) found that the wavelength of the most unstable mode of instability could be found from the ratio of the radius of the vortex cores (r_c, or $c/2$ in Crow's notation) to their separation distance (b_0). A result frequently used from his analysis is that for $r_c/b_0 = 0.098$ (or $d/b_0 = 0.063$ in the notation of Crow's paper), the fastest growing mode of instability is symmetric, has a wavelength of $8.6b_0$, increases in amplitude with a growth period (or e-folding time) of $T = 1.21b_0/W_0$ (where W_0 is the initial vertical velocity of the vortex tubes), and evolves on each tube in a plane tilted at 48° from the horizontal (for a vertically-propagating vortex pair). Moore (1972) later showed that even after the instability reaches large (and hence, nonlinear) amplitudes, it continues to grow with its properties in rough agreement with the linear theory, even until the time at which the two vortex tubes come into contact with one another.

There has been longstanding interest (e.g. Lissaman *et al.* 1973) in how ambient conditions such as stratification, mean shear, and turbulence affect the growth of the Crow instability (and the subsequent vortex ring formation and evolution). In his recent review, Spalart (1998) discusses two different approaches used to investigate these issues in the context of air safety: the predictable decay (PD) view, in which the strength of the vortices is assumed to gradually decay to a safe level within a time estimated straightforwardly from the environmental conditions (see, e.g. Crow & Bate 1976 and Greene 1986), and the stochastic collapse (SC) view, in which the strength of the vortices is assumed to remain constant until instability processes or other effects initiated by the environmental conditions or non-uniformity of the vortices act to dissipate the kinetic energy. We believe in the SC view, and for our laminar numerical simulations the circulation of the vortex tubes is indeed conserved (less a small total loss caused by cross-diffusion – see § 4.1) until baroclinically produced vorticity (formed due to the ambient stratification) interacts with the vortices (see § 4.2).

Most work investigating the effects of ambient stratification on vertically propagating vortex pairs has unfortunately been limited to the study of two-dimensional vortex pairs, which cannot undergo the three-dimensional Crow instability. Recent numerical simulations by Schilling, Siano & Etling (1996), Spalart (1996), Garten (1997), and Garten *et al.* (1998) have shown that weak ambient stratification ($Fr \geqslant 1$) causes a decrease in separation distance and subsequent acceleration of laminar two-dimensional vortex pairs, in general agreement with the predictions of Crow (1974) and Scorer & Davenport (1970), and the experimental results of Tomassian (1979). However, this two-dimensional result may not be relevant to three-dimensional flows because the three-dimensional Crow instability may dominate the evolution on a time scale that precludes the two-dimensional acceleration. In fact, we know of no instances in which acceleration of a three-dimensional vortex pair in ambient stratification has been observed in laboratory experiments (e.g. Sarpkaya 1983) or numerical simulations (e.g. Robins & Delisi 1997). For the three-dimensional solutions reported here, we also find no acceleration of three-dimensional vortex pairs; however, we do find that the decrease in separation distance persists from the two-dimensional case, and that this influences the growth of the Crow instability (and the subsequent evolution).

Schilling *et al.* (1996) and Garten *et al.* (1998) also found that the flow of a two-dimensional vortex pair in ambient stratification is susceptible to secondary instabilities. The vortex head instability results in a growing oscillation of the vortex pair propagation direction about the vertical, while the baroclinically generated wake of the vortex pair is susceptible to jet instabilities. Whether or not these instability processes are relevant to turbulent flows is also an open question at present, as well as whether or not they can influence the evolution of a three-dimensional vortex pair which undergoes the Crow instability.

Regardless of how the growth of the Crow instability is affected by environmental conditions, if it reaches a large enough amplitude for portions of the two vortex tubes to come into close contact, then vortex reconnection will commence. A superficial view of this process is that cross-diffusion viscously cancels anti-parallel vorticity from the two tubes, and reconnected vorticity then connects one vortex tube to the other. Typically, two long anti-parallel vortex tubes will be rearranged into a series of vortex rings via this process.

Aside from its possible role in the evolution of aircraft trailing vortices, vortex reconnection has been conjectured to play important roles in the mixing and production of turbulence, helicity, and aerodynamic noise (Hussain 1986). Some work on the general topic of vortex connection has been done in the context of colliding vortex rings, including Fohl & Turner (1975), Ashurst & Meiron (1987), Oshima & Izutsu (1988), Kida, Takaoka & Hussain (1989, 1991*a*), and Aref & Zawadzki (1991). However, most work has been done in the context of anti-parallel vortex tubes undergoing reconnection in a laminar, incompressible, unstratified, and unsheared fluid, including Pumir & Kerr (1987), Melander & Hussain (1989), Buntine & Pullin (1989), Kerr & Hussain (1989), Saffman (1990), Kida *et al.* (1991*a*), and Shelley, Meiron & Orszag (1993), the last of which included a summary of models that predict the *Re* dependence of the time scale for reconnection. We are unaware of any previous attempts to characterize the *Fr* dependence of this time scale, and in fact, the only work of which we are aware that explicitly discusses the reconnection of anti-parallel vortex tubes in a different (e.g. stratified, sheared, and/or turbulent) background is the compressible calculations of Virk, Hussain & Kerr (1995). We stress that Virk *et al.* discussed a compressible effect which increases the reconnection time scale, while we discuss a stratification effect which decreases the reconnection time scale (see § 4).

In a recent review (Kida & Takaoka 1994), the important differences between scalar, vortex, and vorticity reconnections were discussed, as well as the need for more precise definitions for vortices and eddies. Following those definitions, we will refer to scalar and vortex reconnections, respectively, when the topology of iso-surfaces of a passive scalar or the vorticity magnitude changes, and vorticity reconnection when the topology of vorticity lines changes. Following Jeong & Hussain (1995), we use volume renderings of negative values of λ_2, the second eigenvalue of the symmetric matrix $\boldsymbol{S}^2 + \Omega^2$, to identify and visualize the vortices. We show an overview of the unstratified simulation with $Re = 942$ in figure 1. Unfortunately, because λ_2 is based on flow rotation, vortex *sheets* are not prominently displayed via this method, even if their vorticity is large. Since sheets of baroclinically produced vorticity play an important role in the evolution of the stratified cases, we use volume renderings of both λ_2 and $|\omega|$ to show an overview of the $Fr = 2$ case in figure 2 (see figures 12 and 13 for examples of cross-sectional cuts of the stratified flows).

The remainder of the paper is organized as follows: in § 2, we outline our numerical model and our initial conditions. In § 3, we address the effects of ambient stratification on the development of the Crow instability, while in § 4, we discuss the reconnection phase of the evolution. In § 5, we estimate the critical *Fr* that separates the different regimes of behaviour outlined in § 3 and § 4. In § 6, we summarize our main conclusions.

2. Numerical model

2.1. *Basic equations and numerical method*

We use a numerical model based on the Boussinesq approximation to the three-dimensional Navier–Stokes equations. The full density ($\tilde{\rho} = \bar{\rho} + \rho$) and temperature

($\tilde{T} = \bar{T} + T$) are expanded in terms of horizontal mean (overbar) and perturbation quantities.† The equation of state that relates the two fields is

$$\frac{\rho}{\rho_0} = -\alpha T, \tag{2.1}$$

where α is the thermal expansion coefficient and ρ_0 is a reference value. The background temperature is $\bar{T} = \beta z$, and the buoyancy frequency is then $N = \sqrt{g\alpha\beta}$, where g is the acceleration due to gravity.

A pseudo-spectral, streamfunction/vorticity, Galerkin method (e.g. Canuto *et al.* 1988) is used to solve the system of equations, where the field variables are represented with Fourier polynomials of the form

$$A(x,y,z,t) = \sum_{l=-N_x/2}^{N_x/2} \sum_{m=-N_y/2}^{N_y/2} \sum_{n=-N_z/2}^{N_z/2} \hat{A}_{lmn}(t) \mathrm{e}^{2\pi \mathrm{i}}(l_x/L_x) \mathrm{e}^{2\pi \mathrm{i}}(m_y/L_y) \mathrm{e}^{2\pi \mathrm{i}}(n_z/L_z), \tag{2.2}$$

where N_x, N_y, and N_z are the number of collocation points in the x-, y-, and z-directions, and L_x, L_y, and L_z are the domain lengths. Differentiation of a variable is then accomplished with multiplication by a k-vector in Fourier space, and dealiasing with the 2/3 rule is used in all spatial directions (Canuto *et al.* 1988).

Efficiency is gained by time-advancing only the vertical components of the velocity and the vorticity fields. One non-dimensional form (the non-dimensionalization will be discussed in the next section) of this set of equations is

$$\nabla \cdot \boldsymbol{v} = 0, \tag{2.3}$$

$$\frac{\partial}{\partial_t} \nabla^2 w = \boldsymbol{z} \cdot \nabla \times \nabla \times (\boldsymbol{\omega} \times \boldsymbol{v}) + \frac{1}{Fr^2} \nabla_\perp^2 T + \frac{2\pi}{Re} \nabla^4 w, \tag{2.4}$$

$$\frac{\partial \omega_z}{\partial_t} = -\boldsymbol{v} \cdot \nabla \omega_z + \boldsymbol{\omega} \cdot \nabla w + \frac{2\pi}{Re} \nabla^2 \omega_z, \tag{2.5}$$

$$\frac{\partial}{\partial_t} \boldsymbol{U}_\perp = -\frac{\partial}{\partial_z} \langle w \boldsymbol{v}_\perp \rangle + \frac{2\pi}{Re} \frac{\partial^2}{\partial z^2} \boldsymbol{U}_\perp, \tag{2.6}$$

$$\frac{\partial T}{\partial t} = -(\boldsymbol{v} \cdot \nabla)(\bar{T} + T) + \frac{2\pi}{Re\, Pr} \nabla^2 T, \tag{2.7}$$

where $\boldsymbol{v} = (u, v, w)$ is the velocity, $\boldsymbol{\omega} = \nabla \times \boldsymbol{v} = (\omega_x, \omega_y, \omega_z)$ is the vorticity, $\perp$ denotes the projection onto the horizontal plane, and $\langle\ \rangle$ denotes the horizontal average.

Although it is actually $\nabla^2 w$ that is time-advanced with (2.4), the spectral coefficients of w are trivially found from the spectral coefficients of $\nabla^2 w$ through the relationship

$$\hat{w}_{lmn} = -\frac{1}{k^2} [\nabla^2 w]_{lmn}, \tag{2.8}$$

where $k_x = 2\pi l/L_x$, $k_y = 2\pi m/L_y$, $k_z = 2\pi n/L_z$, and $k^2 = k_x^2 + k_y^2 + k_z^2$ (note that $\hat{w}_{000} = 0$).

The other four components of the velocity and the vorticity fields must be known at each time to advance the solution, and they are found from w and ω_z through the following method. A general velocity field (satisfying (2.3)) may be written in terms of two streamfunctions (ψ and ϕ) and the mean horizontal velocity ($\boldsymbol{U}_\perp(z)$):

$$\boldsymbol{v} = \nabla \times \boldsymbol{\psi} + \nabla \times \nabla \times \boldsymbol{\phi} + \boldsymbol{U}_\perp(z), \tag{2.9}$$

---

† The model also permits unstratified simulations for comparison to the stratified cases.

where $\boldsymbol{\psi} = \psi\hat{\boldsymbol{z}}$ and $\boldsymbol{\phi} = \phi\hat{\boldsymbol{z}}$. This expansion is inherently divergence-free and implicitly satisfies the incompressibility constraint. It can be shown that $w = -\nabla_{\perp}^2\phi$ and $\omega_z = -\nabla_{\perp}^2\psi$, and the spectral coefficients of ψ and ϕ are then found from the spectral coefficients of w and ω_z through the relationships

$$\hat{\psi}_{lmn} = \frac{1}{k_x^2 + k_y^2}\hat{\omega}_{zlmn}, \tag{2.10}$$

$$\hat{\phi}_{lmn} = \frac{1}{k_x^2 + k_y^2}\hat{w}_{lmn}. \tag{2.11}$$

It can further be shown that

$$u = \frac{\partial\psi}{\partial y} + \frac{\partial^2\phi}{\partial x\partial z} + u_{\perp}(z), \tag{2.12}$$

$$\boldsymbol{v} = -\frac{\partial\psi}{\partial x} + \frac{\partial^2\phi}{\partial y\partial z} + \boldsymbol{v}_{\perp}(z), \tag{2.13}$$

and so the non-mean parts of u and $\boldsymbol{v}$ can be found from w and ω_z (through ψ and ϕ) at each time. The mean parts of u and $\boldsymbol{v}$ ($\boldsymbol{U}_{\perp}$) are time-advanced via (2.6). The remaining components of the vorticity are then directly calculated from derivatives of the velocity field, and solutions are obtained by time-advancing (2.4)–(2.7).

We use a hybrid implicit/explicit third-order Runge–Kutta scheme developed by Spalart, Moser & Rogers (1991) to time-advance the variables. Diffusive and buoyancy terms are handled implicitly in spectral space, while nonlinear terms are treated explicitly in physical space, then projected to Fourier space using fast Fourier transforms (FFTs); dealiasing with the 2/3 rule is used in all spatial directions. The timestep δt is variable, selected in accord with the maximum velocity/grid-spacing ratio $\boldsymbol{U} = \max|u/\delta r|$ (u is one component of the flow velocity and δr the grid spacing parallel to that velocity) and the Courant–Friedrichs–Lewy (CFL) condition, $\delta t = \mathrm{CFL}/\boldsymbol{U}$. We use the value of $\mathrm{CFL} = 0.68$ for the full, 3-level Runge–Kutta timestep.

Resolution requirements for our solutions are time-dependent, increasing (or decreasing) by a factor of four or more during the flow evolution. Interpolation (or deterpolation) of field variables allows frugality with finite numerical resources, and is accomplished by expressing the field variables in Fourier space and adding zeros for the coefficients of the new, higher wavenumber modes (or simply setting to zero coefficients above the new highest wavenumber).

The boundary conditions in each direction may be chosen to be either periodic or stress-free with zero normal velocity. In all of our cases, the boundary conditions are periodic in the vertical direction and in the direction parallel to the axes of the vortex tubes. The boundary conditions in the spanwise direction (i.e. perpendicular to the axes of the vortex tubes) are stress-free, and the (left/right) symmetry of the flow is taken advantage of through computing only half of the total solution (we note that the potential for the vortex head instability and sinuous-mode wake instabilities is thus lost).

With computational boundaries, these simulations differ from the ideal case of infinite spatial extent. In particular, an infinite number of image vortices are present, and they contribute to the velocity field of the primary vortex pair, changing it from the infinite domain state. Although the differences may remain small throughout the evolution of the flow, they may be important when comparisons are made to theoretical predictions, laboratory experiments, or other numerical simulations which use different size computational domains.

2.2. *Initial conditions and non-dimensionalizations*

To model a pair of anti-parallel vortex tubes, we use Gaussian distributions of vorticity, centred about axes which are initialized in a perturbed (though symmetric) configuration. A general specification of the initial coordinates of the vortex tubes is given by

$$\left.\begin{aligned} y_1(x) &= y_{10} - \sum_{n=1}^{N_m} a(n)\sin(2\pi n x/L_x + \phi(n))\cos(\Theta),\\ z_1(x) &= z_{10} + \sum_{n=1}^{N_m} a(n)\sin(2\pi n x/L_x + \phi(n))\sin(\Theta),\\ y_2(x) &= y_{20} + \sum_{n=1}^{N_m} a(n)\sin(2\pi n x/L_x + \phi(n))\cos(\Theta),\\ z_2(x) &= z_{20} + \sum_{n=1}^{N_m} a(n)\sin(2\pi n x/L_x + \phi(n))\sin(\Theta), \end{aligned}\right\} \tag{2.14}$$

where N_m is the number of symmetric perturbations of the vortex tubes, $a(n) = a_0 n^{-p}$ (for some $p > 0$) is the amplitude of each perturbation mode, $\phi(n)$ is the phase shift for each perturbation mode, and Θ is the angle through which each perturbed vortex is tilted from the horizontal. For all of the cases reported here, $N_m = 1$, $a(1) = 0.05$, $\phi(1) = 0$, and $\Theta = 48°$. The unperturbed positions of the two vortices are (y_{10}, z_{10}) and (y_{20}, z_{20}); $y_{20} - y_{10} = b_0$, the initial vortex core separation distance, and $z_{20} = z_{10}$.

Since the positions of the vortex tubes are initially perturbed in this manner, the initial distribution of ω_x is $\hat{x}$-dependent, and ω_y and ω_z are non-zero. Our specification of the initial vorticity field† is

$$\left.\begin{aligned} \omega_x(x,y,z,t=0) &= \omega_0(\mathrm{e}^{-\rho_1^2/2\sigma^2} - \mathrm{e}^{-\rho_2^2/2\sigma^2})\cos(\zeta),\\ \omega_y(x,y,z,t=0) &= -\omega_0(\mathrm{e}^{-\rho_1^2/2\sigma^2} + \mathrm{e}^{-\rho_2^2/2\sigma^2})\sin(\zeta)\cos(\Theta),\\ \omega_z(x,y,z,t=0) &= \omega_0(\mathrm{e}^{-\rho_1^2/2\sigma^2} - \mathrm{e}^{-\rho_2^2/2\sigma^2})\sin(\zeta)\sin(\Theta), \end{aligned}\right\} \tag{2.15}$$

where

$$\left.\begin{aligned} \rho_1^2 &= (y - y_{10}(x))^2 + (z - z_{10}(x))^2,\\ \rho_2^2 &= (y - y_{20}(x))^2 + (z - z_{20}(x))^2,\\ \zeta &= \sum_{n=1}^{N_m} n a(n)\cos(2\pi n x/L_x + \phi(n)), \end{aligned}\right\} \tag{2.16}$$

σ is a vortex core size, and ω_0 is the peak magnitude of vorticity (all of our cases are for descending vortex pairs, and so $\omega_0 < 0$). As mentioned in the previous section, the symmetry of the flow may be used by not computing the entire solution, and the initial conditions are modified appropriately.

All of our simulations are performed with a non-dimensional set of equations. Length, velocity, and temperature are reported in units of b_0, W_0, and β, where W_0

---

† This specification of the initial vorticity field only obeys $\nabla\cdot\boldsymbol{\omega} = 0$ to order σ^2/b_0^2. However, the small errors (order 10^{-4}) introduced by this approximation do not appear to significantly affect the evolution.

is the magnitude of the initial vertical induced velocity and β is the background temperature gradient. Other quantities are measured in units resulting from combinations of these three variables, e.g. time is reported in units of b_0/W_0. Important combinations of these and other parameters form non-dimensional quantities which we use to characterize our solutions. These include Fr, Re, and Pr (Prandtl number), which are now defined.

The Froude number (or inverse stratification number) is defined as

$$Fr = \frac{W_0}{Nb_0}, \tag{2.17}$$

where N is the buoyancy frequency of the background stratification. Hence, Fr is the ratio of the buoyancy timescale to the vortex-pair advection timescale. In the nonlinear regime ($Fr > 1$) the advective effect of each vortex on the other is greater than buoyancy effects, while in the linear regime ($Fr < 1$) the opposite is true. The labels linear and nonlinear refer to the nature of the underlying flow equations in these regimes.

The Reynolds number,

$$Re = 2\pi \frac{W_0 b_0}{\nu}, \tag{2.18}$$

is the ratio of the viscous timescale (b_0^2/ν) to the advective timescale (b_0/W_0), where ν is the coefficient of kinematic viscosity. The 2π factor is included here because in the literature the Reynolds number is often defined in terms of the initial circulation, $\Gamma_0 = 2\pi W_0 b_0$. The number of grid points used limits the value of Re that can be attained numerically. In order to investigate the implications of the constraint for Re, we have performed unstratified simulations at $Re = 628$, 942, and 1260.

The Prandtl number, $Pr = \nu/\kappa$, is the ratio of the diffusive timescale (b_0^2/κ) to the viscous timescale (b_0^2/ν). The value of Pr determines how quickly thermal gradients diffuse relative to velocity gradients, and we have used $Pr = 1$ to prevent the numerical resolution requirements of our solutions from escalating out of control.

For all of the simulations reported here, the vortex core size is $\sigma/b_0 = 0.0707$; for this choice, the vortices are small enough to be distinct entities but large enough to be adequately resolved in the computations (see table 1). A solid core vortex with the same peak magnitude of vorticity and the same total circulation would have a radius $r_c = 0.1$, and hence a Crow (1970) cutoff distance of $d = 0.064$.

To prevent significant interaction with the image vortices, the width of the computational domain L_y is made large compared to b_0; specifically we choose $L_y = 8b_0$ (or $4b_0$ for the half-domain) for the unstratified cases, and $L_y = 16b_0$ for the stratified cases. The height of the computational domain L_z must be large enough to prevent the vortices from encountering image vorticity; we use $L_z = 8b_0$ for the unstratified cases, and $L_z = 10.67b_0$ for the stratified cases. A taller domain is needed for the stratified runs because of the rebounding motion of some of the fluid initially displaced by the vortex tubes.

As discussed in Garten *et al.* (1998), we continue to lack a reliable method for quantitatively determining the quality of numerical resolution of our solutions. We therefore use the method of looking for Gibbs' oscillations and/or numerical ringing throughout the flow evolutions, and do not allow such ringing to reach visible amplitudes (see e.g. figures 12 and 13).

Flow parameters			Domain lengths			Spectral modes			
Fr	Re	Pr	L_x	$L_y/2$	L_z	N_x	N_y	N_z	$(\sigma/b_0)N_y$
∞	628	1	8.6	4	8	128	128	256	2.3
∞	942	1	8.6	4	8	256	192	384	3.4
∞	942	1	8.6	8	8	256	384	384	3.4
∞	1260	1	8.6	4	8	256	256	512	4.5
∞	2200	1	8.6	4	8	128	128	256	2.3
∞	3140	1	8.6	4	8	256	256	512	4.5
8	942	1	8.6	8	10.67	256	384	512	3.4
4	942	1	8.6	8	10.67	256	384	512	3.4
2	942	1	8.6	8	10.67	256	384	512	3.4
1	942	1	8.6	8	10.67	256	384	512	3.4
1/2	942	1	8.6	8	10.67	256	384	512	3.4
2	942–3140	1		8	10.67		384	512	3.4
2	6280	1		8	10.67		768	1024	6.8
1	942	1		8	10.67		384	512	3.4
0.725–0.8	9420	1		8	10.67		768	1024	6.8
0.65–0.725	942	7		8	10.67		768	1024	6.8
0.6–0.7	942	1		8	10.67		384	512	3.4
1/2	942	1		8	10.67		384	512	3.4

TABLE 1. The values of the flow parameters, computational domain lengths, and maximum numerical resolutions of the numerical simulations we describe here. Note that the product $(\sigma/b_0)N_y$ yields the number of grid points per core radius (σ), and that the $Re = 2200$ and $Re = 3140$ cases were computed with the filtering method described in § 2.3. In all cases, $\sigma/b_0 = 0.0707$.

2.3. *Comments regarding our large grid sizes*

We place great importance on completely resolving our solutions for all time; however, strong constraints then exist on what aspects of the general problem we can hope to explore. As can be inferred from the number of spectral modes used in these simulations (see table 1), it is not practical for us to attempt studies incorporating significantly longer vortex tubes (and thereby allowing the dominant wavelength of the instability to evolve) or larger Re. However, some investigators have utilized numerical filtering techniques (e.g. Robins & Delisi 1996, 1997), hyperviscosity regularization (e.g. Boratav, Pelz & Zabusky 1992), and subgrid scale methods (e.g. Corjon *et al.* 1996) to overcome these obstacles in related studies of three-dimensional vortices interacting under different environmental conditions.

We have made comparisons with our own code between our $Re = 1260$ run and under-resolved (the resolution was decreased by a factor of 4 in each spatial direction) and filtered (the highest 1/2 wavenumbers were zeroed every 30 time steps for the smaller-resolution run) solutions. We find that the time evolution of quantities such as the amplitude of the Crow instability, the fraction of circulation that has reconnected, and the spatial positions of the vortex tubes and the subsequently formed vortex ring change by only a few percent or less. Therefore, one possible view is that this work thus helps validate those smaller resolution approaches (at least for $Re = 1260$, and perhaps for larger Re) in situations where there is interest in these qualitative aspects of the flow.

However, when we employed these smaller-resolution techniques, a significant amount of numerical ringing built up over time in our solutions. The details of

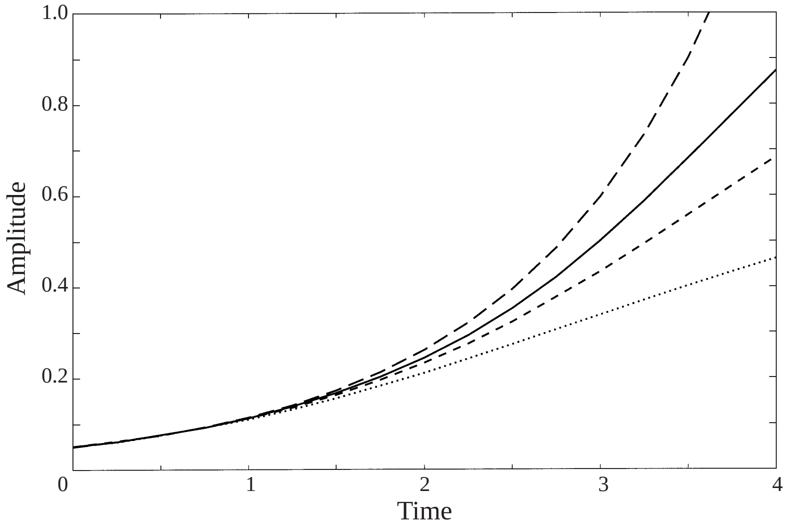

FIGURE 3. The time evolution of the instability amplitude for the unstratified cases with $Re = 628$ (dotted), $Re = 942$ (short-dashed), and $Re = 1260$ (solid), compared to the theoretical prediction of Crow's model (long-dashed).

the vortex reconnection process as well as aspects of the late time evolution also hold interest for us, and so in this and future studies we continue to use large maximum grid sizes in order to maintain numerical accuracy as fully as possible throughout the evolution.

3. The Crow instability in a viscous, stratified fluid

We begin our discussion of the results with an examination of the Crow instability phase of the evolutions. For our vortex core size (slightly different from the classical Crow value – a small error not discovered until too late), Crow's inviscid theory predicts that the fastest growing mode of instability is symmetric, has a wavelength of $8.5b_0$, a growth period of $T = 1.21$, and evolves on each tube in a plane tilted at 47.5° from the horizontal. Although the perturbations on our vortex tubes are initialized at an angle of 48° from the horizontal, and with an imposed wavelength of $8.6b_0$ (the classical Crow values), the predicted growth period is still $T = 1.21$ (to three significant digits).

3.1. *The Crow instability in a viscous fluid*

As we are interested in the effects of environmental factors, like ambient stratification, on the growth of the Crow instability, we first consider how it evolves in the absence of external effects. We show the time evolution of the instability amplitude for our three unstratified cases in figure 3. These results show clearly that the agreement with Crow's model improves for larger *Re*. Our explanation for the slower growth of the instability for smaller *Re* begins with the fact that the vortex core size increases noticeably during the Crow instability phase. As discussed in Garten *et al.* (1998), to a good approximation, the core size of the vortices increases as

$$\sigma(t) = \left[\sigma(0)^2 + \frac{4\pi}{Re}t\right]^{1/2}. \tag{3.1}$$

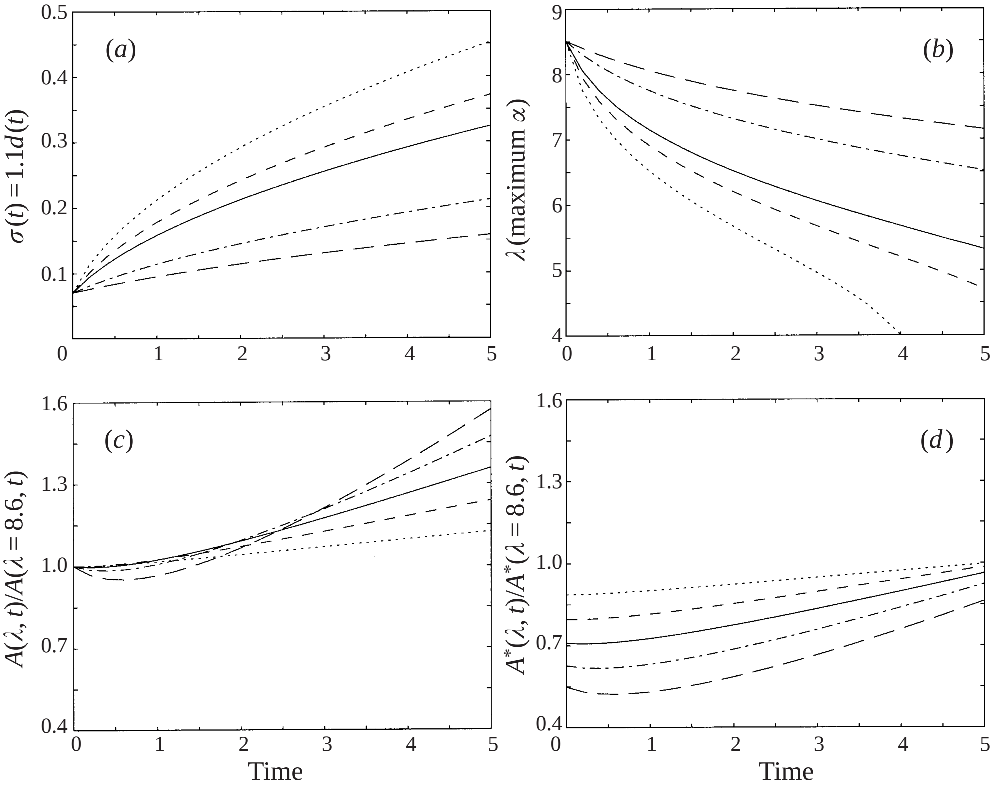

FIGURE 4. (*a*) The time evolution of σ for $Re = 628$ (dotted), $Re = 942$ (short-dashed), $Re = 1260$ (solid), $Re = 3140$ (dot-dashed), and $Re = 6280$ (long-dashed). Note that $\sigma(0) = 0.0707$. (*b*) The time evolution of the wavelength of the fastest growing linear mode for the same values of Re as in (*a*). (*c*) The time evolution of the amplitude of the linear modes, for $Re = 942$, with wavelengths $\lambda = 8.0b_0$ (dotted), $\lambda = 7.5b_0$ (short-dashed), $\lambda = 7.0b_0$ (solid), $\lambda = 6.5b_0$ (dot-dashed), and $\lambda = 6.0b_0$ (long-dashed). The different modes are initialized with the same amplitude, and the amplitudes are normalized by the *time-dependent* amplitude of the linear mode with $\lambda = 8.6b_0$. (*d*) Same as (*c*), except that the initial amplitude of the modes decreases as $\lambda^{5/3}$.

Examples of how quickly σ grows as given by (3.1) are shown in figure 4(*a*). Note that for our particular simulations, significant vortex reconnection begins to occur by $t \simeq 3.5$ (see §4.1).

The general implications of an evolving vortex core size for the Crow instability are not necessarily clear. One possibility is to take the naive approach that the growth rates of all the linear modes depend straightforwardly on the vortex core size at each instant in time. However, the wavelength of the fastest growing mode (as given by Crow's inviscid model) would then be time dependent, as shown in figure 4(*b*). In general, if initial perturbations are sufficiently weak for one mode to not grow quickly to a finite (nonlinear) amplitude†, this shift could result in the emergence of an instability with a different wavelength than expected from the initial state.

To explore such possible shifts, we use our naive assumption that a growth rate for a mode at each instant in time can be found directly from the core size at each instant in time to calculate the amplitudes of selected linear modes that are all evolving

---

† The most general problem is complicated further by this unknown timescale, while our particular simulations are initialized with finite amplitudes.

at $Re = 942$. We normalize the amplitudes by the *time-dependent* amplitude of the mode with $\lambda = 8.6b_0$ (so that some mode amplitudes appear to decrease initially but merely increase at a slower rate), and their time evolutions are shown in figures 4(*c*) and 4(*d*). In the first case, all the modes are initialized with identical amplitudes, and, at this *Re*, smaller-wavelength modes actually gain greater amplitudes than the default mode. Depending on how long it takes for one mode to attain a finite (nonlinear) amplitude (for these purposes, the e-folding timescale for all of these modes is $O(1)$), it is difficult to predict what dominant wavelength would emerge. In the second case, however, the modes are initialized with wavelength-dependent amplitudes. Unfortunately, any particular choice for the functional dependence of the initial amplitude is difficult if not impossible to justify (Robins 1998, Spalart 1998, private communications). We believe that larger wavelengths will in general be excited initially with larger amplitudes, and use the particular functional dependence $\lambda^{5/3}$ to illustrate the possible consequences when this general assumption is true. In particular, the mode with $\lambda = 8.6b_0$ now retains the largest amplitude for all time.

Although these points raise interesting questions about the evolution of the Crow instability in general small-*Re* flows (Robins & Delisi 1997 have reported multiple wavelength studies in which they find the dominant wavelength indeed shifts with time), the implications for our particular simulations appear to be more straightforward. We initialize a finite- (nonlinear) amplitude perturbation on our vortex tubes, and there is also only a discrete spectral range of modes available to the solution (the next closest mode is the one with $\lambda = 4.3b_0$). Therefore, the solution cannot realistically shift to a different wavelength. However, we can expect that the growth *rate* of the instability slows as the vortex core size increases (with our assumptions, the growth rate at any time will depend on the vortex core size at that moment in time).

We have calculated the expected growth of the instability (i.e. the time evolution of the amplitude as well as the mean inclination angle of the vortex tube displacements) for our three *Re* from both points of view that it is (dotted lines) and is not (long-dashed lines) affected by the core size increase in the way just outlined, and the results are shown in figures 5(*a*) and 5(*b*). Note that the difference between these predictions decreases for larger *Re*, because the core size increases less rapidly for larger *Re*. Because the vortex tubes distort from their initial sinusoidal shape as the instability evolves†, it is difficult to decide how to measure the actual amplitude of the instability. We first determine the locations (the (y, z)-positions) of the centroids of the vortex tubes at each x-position, and project all of these points onto one plane to determine the mean inclination angle of the vortex tube displacements. The time evolution of this actual mean inclination angle is shown in figure 5(*a*) (triangle symbols), and in each case it increases consistently with the prediction of the extended model.

We then measure the vortex tube displacements at the positions of furthest separation (star symbol) and closest approach (diamond symbol) of the vortex tubes and project them onto the plane of mean inclination to make two measurements of the instability amplitude (the average of these measurements is used in figure 3), and we show these measurements in figure 5(*b*). Figure 5(*c*) shows displacements perpendicular to the mean inclination plane (multiplied by 5 for display purposes), and these measurements indicate that the distortion increases slightly for larger *Re*.

---

† As mentioned by Moore (1972), the vertical advection of the vortex tubes depends on their separation distance; once this distance significantly varies along the tubes, the vertical propagation becomes non-uniform, and shape distortion results.

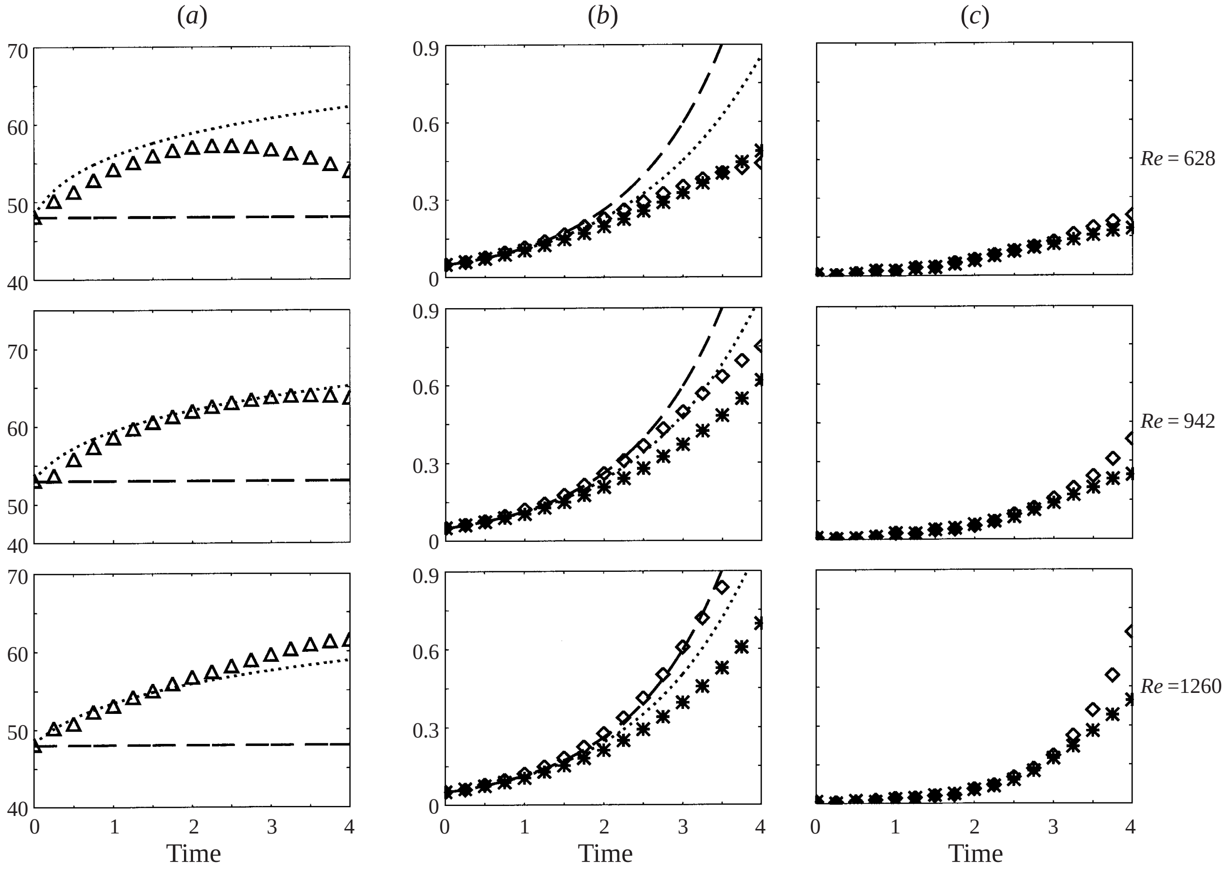

FIGURE 5. The time evolutions of (*a*) the mean inclination angle of the vortex tube displacements, (*b*) the amplitude of the displacements projected onto the plane of mean inclination, and (*c*) the amplitude of the displacements perpendicular to this plane (multiplied by 5 for display purposes), for the unstratified cases with $Re = 628$ (top), $Re = 943$ (middle), and $Re = 1257$ (bottom). The vortex core displacements have been measured at the positions of furthest separation (star symbol) and closest approach (diamond symbol) of the vortex tubes, and comparisons to the predictions of the original (dashed) and modified (dotted) Crow models are shown.

We note that although all of these measurements are shown up to $t = 4$, significant vortex reconnection commences by $t \simeq 3.5$ (see § 4.1). The overall agreement with the theory extension is worst for the $Re = 628$ case, but improves for larger Re. We note that most of the distortion results from a variation in the vertical propagation of the vortex tubes caused by the variation in separation distance along the tubes (i.e. the tubes are elongated in the vertical direction); therefore, the instability amplitude is henceforth calculated by projecting the horizontal displacements only onto the plane of mean inclination.

3.2. *The Crow instability in a stratified fluid*

We now consider how ambient stratification affects the development of the Crow instability. A simple timescale analysis leads us to expect that this part of the evolution should not change for large Fr (recall that the unstratified limit corresponds to $Fr \to \infty$). Effects due to the stratification should only occur over timescales on the order of the buoyancy period, and in the non-dimensional time units the buoyancy period is $2\pi/N = 2\pi Fr$. Because of the large amplitude we use to initialize the perturbations on the vortex tubes, the instability reaches a large enough amplitude to result in significant vortex reconnection by about $t \simeq 3.5$ (see § 4.2); therefore, we should not expect the Crow instability phase of the evolution to change unless Fr is $O(1)$ or less.

The time evolution of the instability amplitude, as measured by the method just discussed, is shown in figure 6 for several values of Fr. These measurements are compared to the prediction of the extended theory discussed in the previous section (dotted lines), where in all of these cases $Re = 942$. As expected, the growth of the instability for the $Fr \geqslant 2$ cases is nearly identical to the unstratified ($Fr \to \infty$) case. However, the instability grows noticeably faster for the $Fr = 1$ case, and noticeably slower for the $Fr = 1/2$ case. We note that the instability reaches an amplitude sufficiently large for the $Fr = 1$ case that the two instability amplitude estimates diverge. This is because the amplitude at the position of closest approach cannot exceed $b/2$ divided by the cosine of the inclination angle. Therefore, after $t \simeq 3$, the amplitude inferred at the position of furthest separation is much more meaningful for the $Fr = 1$ case.

In measuring the instability amplitude for these stratified cases, it is important to take into account that the average horizontal positions of the vortex tubes can be time dependent. Therefore, the vortex tube displacements must be measured with respect to the time-evolving average positions. The results of numerous investigations of the evolution of two-dimensional vortex pairs in a stratified fluid via theory (Scorer & Davenport 1970; Crow 1974) and laminar numerical simulations (Spalart 1996; Schilling *et al.* 1996; Garten 1997; Garten *et al.* 1998)†, provide explanations for changes in the average separation distance of these three-dimensional vortex tubes (because of the flow symmetries, the average separation distance yields straightforwardly the average horizontal position of each vortex tube). Horizontal density gradients result from the downwards transport of relatively lighter fluid by the vortices; these gradients constitute a baroclinic source that produces vorticity behind

---

† We note that results of laboratory experiments (e.g. Sarpkaya 1983) and field experiments involving three-dimensional vortex pairs in stratified fluids are sometimes used to dispute the conclusions of these other works. However, we are not aware of any published experimental results that include measurements of the average horizontal positions (or, equivalently, the average separation distance) of three-dimensional vortex tubes in stratification, and so we have no basis for comparison on this point.

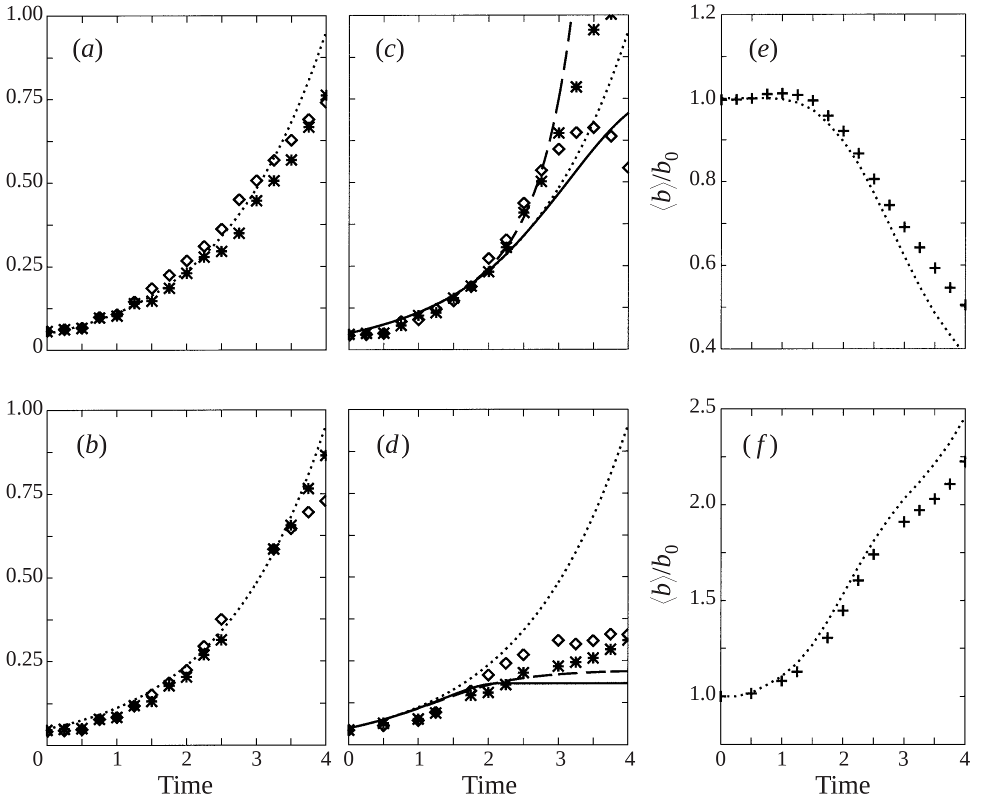

FIGURE 6. The time evolution of the amplitude of the Crow instability as given by the horizontal displacements of the vortex tubes from their average positions for the $Re = 942$ cases with (*a*) $Fr = 4$, (*b*) $Fr = 2$, (*c*) $Fr = 1$, and (*d*) $Fr = 1/2$. The displacements are measured at the positions of closest approach (diamond symbol) and furthest separation (star symbol) of the vortex tubes, and some data is missing for the $Fr = 2$ case due to a supercomputer storage glitch. These measurements are compared to the prediction of the modified theory (dotted lines), where the growth rate decreases as the the core size increases, and, in the $Fr = 1$ and $1/2$ cases, to the time-rescaled theory (long-dashed lines) and the fully rescaled theory (solid lines). For these latter two cases, in (*e*) and (*f*) the time evolution of the average separation distance of the three-dimensional vortex tubes (cross symbols) is compared to the separation distance of a two-dimensional vortex pair at the same *Fr* (dotted lines).

and to the sides of the original vortices (as discussed in greater detail in §4.2). For $Fr \geqslant 1$, these countersign regions of secondary vorticity then advect the primary vortices towards one another, while for $Fr \leqslant 1/2$, they have a qualitatively different distribution and advect the primary vortices away from one another (see Garten *et al.* 1998). The aforementioned simulations of two-dimensional vortex pairs have also shown that there is a time lag before this horizontal motion commences. For our three-dimensional cases with $Fr \geqslant 4$, the average separation distance of the vortex tubes decreases by less than 5%, while for our cases with $Fr \leqslant 2$, more rapid changes transpire.

The time evolution of the average separation distance, $\langle b\rangle$, of the vortex tubes is shown in figure 6(*e*, *f*) for the $Fr = 1$ and $Fr = 1/2$ cases (cross symbols). These results are compared to the results of simulations of two-dimensional vortex pairs at the same *Fr* (dotted lines). Although the three-dimensional dynamics result in some quantitative differences, the evolution of the three-dimensional average separation distance is in good agreement with the evolution of the two-dimensional separation distance. This suggests that if our simulations were initialized with smaller-amplitude perturbations (so that the Crow instability phase would have a longer duration), then the average horizontal movement of the vortex tubes during the three-dimensional Crow instability phase, and the subsequent effect on the growth of the Crow instability, would be greater for all *Fr*.

In view of the success of our naive approach to understanding the growth of the Crow instability in a viscous fluid, we now make a similar attempt to understand the growth of the Crow instability in a stratified fluid. We propose that as $\langle b \rangle$ evolves, the rate of the instability evolution also evolves. Recalling that time is initially scaled by b_0/W_0, and that $W_0 \sim 1/b_0$, we propose that the time scaling of the evolution evolves as $\delta t \simeq 1/\langle b \rangle^2$. We then include this 'acceleration' factor (a deceleration for $Fr \leqslant 1/2$ where $\langle b \rangle$ increases) in our modified Crow model to predict the growth of the instability for our $Fr \sim O(1)$ cases, and these new predictions are shown in figure 6(c, d) (long-dashed lines). The agreement with this extension is generally good; however, as pointed out by one of the anonymous referees, our theory extension does not include the lengthscale shifts (the non-dimensional wavelength: $\lambda \sim 1/\langle b \rangle$, and the vortex core cutoff distance: $d/\langle b \rangle$) that must also occur as $\langle b \rangle$ evolves. Predictions including this effect are also shown in figure 6(c, d) (solid lines), and they are inadequate to explain the observations, especially in the $Fr = 1$ case. A clear and precise explanation for this difficulty continues to elude us. We note that Robins & Delisi (1996) have also reported that the Crow instability proceeds more rapidly in ambient stratification (for $Fr > 1$).

One effect that we neglect is the possible instability-type interactions amongst the original vortices and the regions of baroclinic vorticity. Consideration of the non-uniform distribution of baroclinic vorticity along the vortex tubes (discussed more fully in § 4.2) may also provide additional insights. For the $Fr \geqslant 1$ cases (see e.g. figures 12 and 13), relative to the decrease in $\langle b \rangle$, the vortex tubes have a larger (smaller) effective *Fr* where they are closer together (further apart), and the distribution of baroclinic vorticity is such that the vortex tubes are advected even closer together (further apart). Hence, faster growth of the instability amplitude would ensue. For the $Fr \leqslant 1/2$ cases, the strength of the baroclinic regions of vorticity increases so rapidly that each primary vortex tube falls under the influence of its neighbouring baroclinic vorticity much more than the other primary vortex.

4. The vortex reconnection phase

We now discuss the vortex reconnection phase of the evolutions. We present both unstratified and stratified results to set clearly a consistent context in which to discuss effects due to stratification. Without stratification, time-preserved symmetries allow the vorticity equations to be expressed at the centreplane between the two vortices (i.e. the x, z-plane at $y = 0$) as follows:

$$\omega_x = \omega_z = 0, \tag{4.1}$$

$$\frac{\partial \omega_y}{\partial t} = \frac{2\pi}{Re}\frac{\partial^2 \omega_y}{\partial y^2} + \omega_y \frac{\partial v}{\partial y} - \left(u\frac{\partial \omega_y}{\partial x} + w\frac{\partial \omega_y}{\partial z} \right) + \frac{2\pi}{Re}\left(\frac{\partial^2 \omega_y}{\partial x^2} + \frac{\partial^2 \omega_y}{\partial z^2} \right), \tag{4.2}$$

where the terms of (4.2) are arranged for the purpose of the following discussion. Initially, $\omega_y = 0$ everywhere on the centreplane, and all of the terms on the right of

(4.2) are zero. However, when the instability reaches a sufficiently large amplitude, the first term of (4.2) becomes non-zero, and reconnection can be said to commence. Once this occurs (i.e. ω_y is non-zero on the centreplane), all of the terms of (4.2) can be non-zero, but only the first term contributes a *net change* in circulation (see figure 9, below). It constitutes both a source of spanwise (i.e. $\hat{y}$-oriented) vorticity that arises from the linking and realignment of the unannihilated parts of vortex lines whose middle portions are annihilated by viscous cross-diffusion (Melander & Hussain 1989), as well as a sink of spanwise vorticity that arises from viscous spreading. The second term of (4.2) is a stretching term, the next two terms represent advection of spanwise vorticity within the centreplane, and the final two terms represent viscous spreading of spanwise vorticity within the centreplane. The volumes of vorticity that connect the two vortex tubes through the centreplane have been called bridges (Melander & Hussain 1989), and the rate at which the bridges form is controlled by (4.2).

In addition to integrating ω_y and/or $\partial\omega_y/\partial t$ over half of the centreplane (*two* vortex bridges form where the vortex tubes approach most closely, and they possess anti-symmetry about that point for all time), the rate of vortex reconnection can also be quantified via the following method. The circulation of the positive vortex tube is†

$$\Gamma(x) = \int_0^{L_y/2}\int_0^{L_z} \omega_x(x,y,z)\,\mathrm{d}y\,\mathrm{d}z. \tag{4.3}$$

In the unstratified case, $\Gamma(x)$ decreases only via cross-diffusion at the centreplane:

$$\frac{\partial \Gamma(x)}{\partial t} = -\frac{2\pi}{Re}\int_0^{L_z} \left.\frac{\partial \omega_x}{\partial y}\right|_{(x,0,z)} \mathrm{d}z. \tag{4.4}$$

Although the spatial distribution (on the centreplane) of $(2\pi/Re)$ $(\partial\omega_x/\partial y)$ indicates where annihilation via viscous cross-diffusion occurs (e.g. figure 9), only the spatial distribution of the source part of the first term of (4.2) indicates where reconnection actually occurs (see figure 9). We believe it less important to consider the distribution of cross-diffusion (which occurs along some finite length of the vortex tubes), shown in the middle column of figure 9, than the distribution of 'actual' reconnection, as shown via the overlaid shaded contours in figure 9. Without this distinction, cross-diffusion that occurs everywhere along the tubes would be thought of as reconnecting the entire length of the tubes.

We define Γ_f and Γ_c as the total circulation of the positive vortex tube at the positions of furthest separation and closest approach of the vortex tubes, respectively. Henceforth, the (y,z)-planes at these x locations are referred to as plane f and plane c, respectively. Γ_f is the maximum circulation of the positive vortex tube for all time, and we therefore think of a viscously driven decrease in Γ_f as a decrease in the total circulation (i.e. if Γ_f decreases, then cross-diffusion has occurred everywhere along the vortex tubes). The vast majority of the viscously driven decrease in Γ_c occurs simultaneously with an increase in spanwise circulation (via the first term of (4.2)). This is a simple view of the process of vortex reconnection which ignores the detailed geometries associated with the vorticity reconnection of particular vortex lines – see, e.g. figure 3 of Kida & Takaoka (1994). From these two quantities, we construct a simple measure for the minimum circulation‡ of the positive vortex bridge, which we

---

† For the stratified cases discussed in § 4.2, the positive vortex tube is quickly surrounded by baroclinically produced negative vorticity; therefore, the following area integral is taken only over the region bounded by the zero vorticity line between the primary and background vorticity.

‡ Although it is difficult to define where the vortex tubes end and where the vortex bridges between

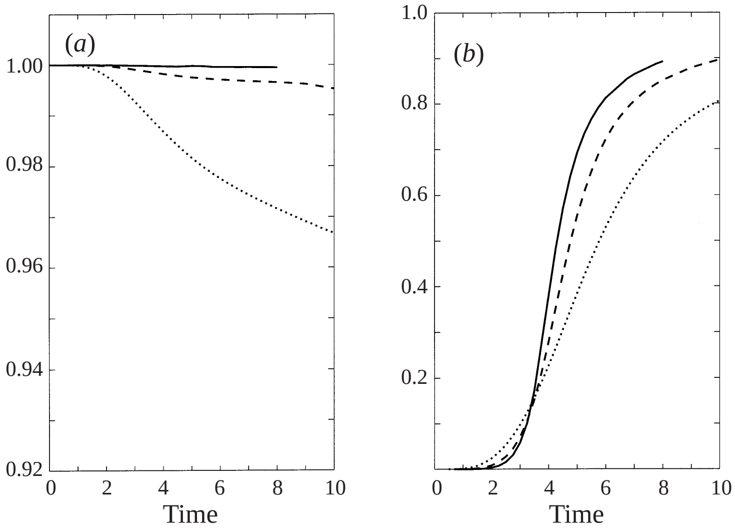

FIGURE 7. The time evolution of the undisturbed circulation of each vortex tube ($\Gamma_f/\Gamma_0, a$) and the fraction of circulation that is reconnected into a vortex ring ($\Gamma_r/\Gamma_f, b$) for the unstratified cases with $Re = 628$ (dotted), $Re = 942$ (dashed), and $Re = 1260$ (solid).

define as Γ_r: $\Gamma_r = \Gamma_f - \Gamma_c$. Although we have confirmed that this measure coincides with a direct measurement of Γ_r in the unstratified cases, we use this indirect method as it is more convenient in complex environments where additional sources (e.g. baroclinic) of spanwise vorticity exist. Of course, $\Gamma_r = \Gamma_f - \Gamma_c$ no longer strictly holds in such cases, but the quantity $1.0 - \Gamma_c/\Gamma_f$ will still indicate the completeness of reconnection.

4.1. *Vortex reconnection in an unstratified fluid*

We first consider the vortex reconnection phase of the evolution without any external effects. The time evolution of Γ_f, normalized by the initial circulation, and the fraction Γ_r/Γ_f are shown in figure 7 for our three different *Re* cases. As seen in the time evolution of Γ_f, there is a small but noticeable total loss of circulation for these tractable values of *Re*. This is a consequence of the increase in size of the vortex cores (through viscous diffusion). Some anti-parallel vorticity cancels where the vortex tubes are furthest apart, even though the growth of the Crow instability results in migration of the vortex core centres away from one another (and the centreplane). As discussed in § 3.1, a larger *Re* results in slower growth for the vortex core size (see figure 8 and figure 10, and in more rapid growth of the instability amplitude (see figure 3). Both of these effects reduce the vorticity gradients at the centreplane where the vortex tubes are furthest apart, and thereby reduce the loss in Γ_f. For increasing *Re*, the percentage of the original circulation that is lost by $t = 8$ in these three simulations is 2.8%, 0.3%, and 0.1%, respectively. In the light of the results summarized in figure 11, it is important to note how very little total circulation is lost in the absence of external effects.

Now consider the time evolution of Γ_r/Γ_f. Initially, the vortex reconnection pro-

them begin, if the vortex bridges are thought of as three-dimensional volumes and not as merely the two-dimensional regions of spanwise vorticity in the centreplane, then the minimum (maximum) circulation of the positive (negative) vortex bridge is the circulation of the two-dimensional region of positive (negative) vorticity.

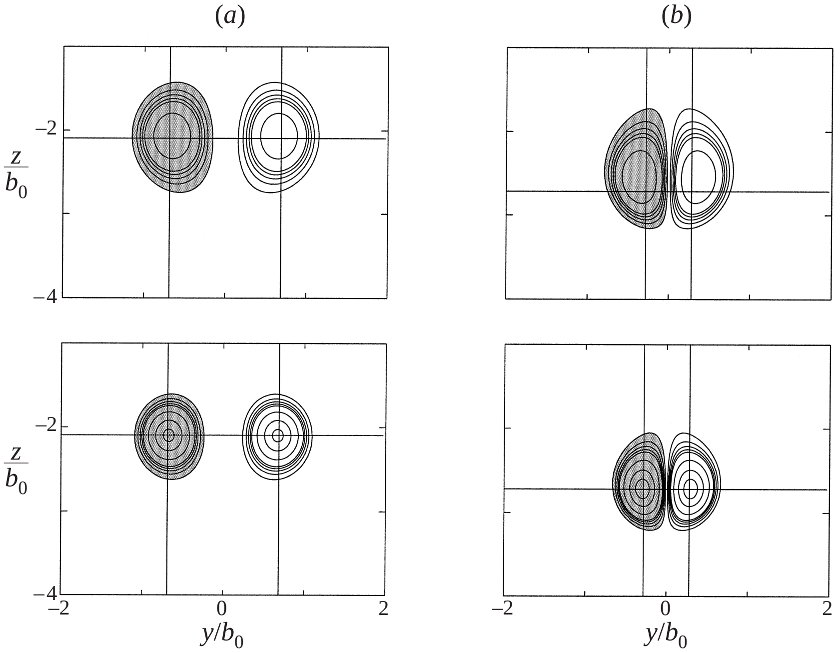

FIGURE 8. Contours of vorticity in planes *f* (*a*) *c* (*b*) of the vortex tubes for the cases with $Re = 628$ (top) and $Re = 1260$ (bottom) at the time $t = 2.5$. Contour levels at $\pm 10, \pm 20, \pm 30$, etc. show the distribution of high-magnitude vorticity, while additional contour levels at $\pm 1, \pm 2, \pm 3, \pm 4, \pm 5$ illustrate the distribution of low-magnitude vorticity. All regions enclosed by negative contours are shaded, and lines have been drawn to show the positions of the vortex tube centres for the $Re = 1260$ case.

ceeds more rapidly for smaller *Re*. Even though the instability growth is slower (see figure 3), and so the centres of the closest portions of the vortex tubes are not as close to the centreplane (see figures 8–10), viscously driven expansion of the vortex cores is faster, and so more anti-parallel vorticity is near the centreplane at early times (i.e. through $t \simeq 3$). Therefore, the gradients of vorticity at the centreplane are initially larger, and their products with $1/Re$ (i.e. the first term of (4.2) and (4.4)) are larger still.

Eventually, however, the faster instability growth for larger *Re* begins to accelerate the vortex reconnection. The centres of the closest portions of the vortex tubes move closer to the centreplane, and the faster buildup of vorticity then steepens the gradients of vorticity at the centreplane. Even though *Re* is larger, so that cross-diffusion might be expected to occur more slowly, it happens more rapidly because the vorticity gradients become much larger. As judged from the crosshairs in figure 9 (not all shown), at $t = 3.5$, the vorticity gradient in plane *c* for the $Re = 1260$ case is roughly 5 and 1.8 times as large as for the $Re = 628$ and $Re = 942$ cases, respectively.

As observed and discussed in numerous numerical investigations of vortex reconnection (including Pumir & Kerr 1987; Melander & Hussain 1989; Buntine & Pullin 1989; Kerr & Hussain 1989; Kida *et al.* 1991*a*,*b*; Shelley *et al.* 1993; and Virk *et al.* 1995), a point is reached at which anti-parallel vorticity builds up near the centreplane more quickly than it can be eliminated via cross-diffusion. As a result, the vortex cores deform into a 'head–tail' distribution (Kida *et al.* 1991*b*). Vortex stretching increases the maximum value of vorticity and narrows the vortex cores (via the second to

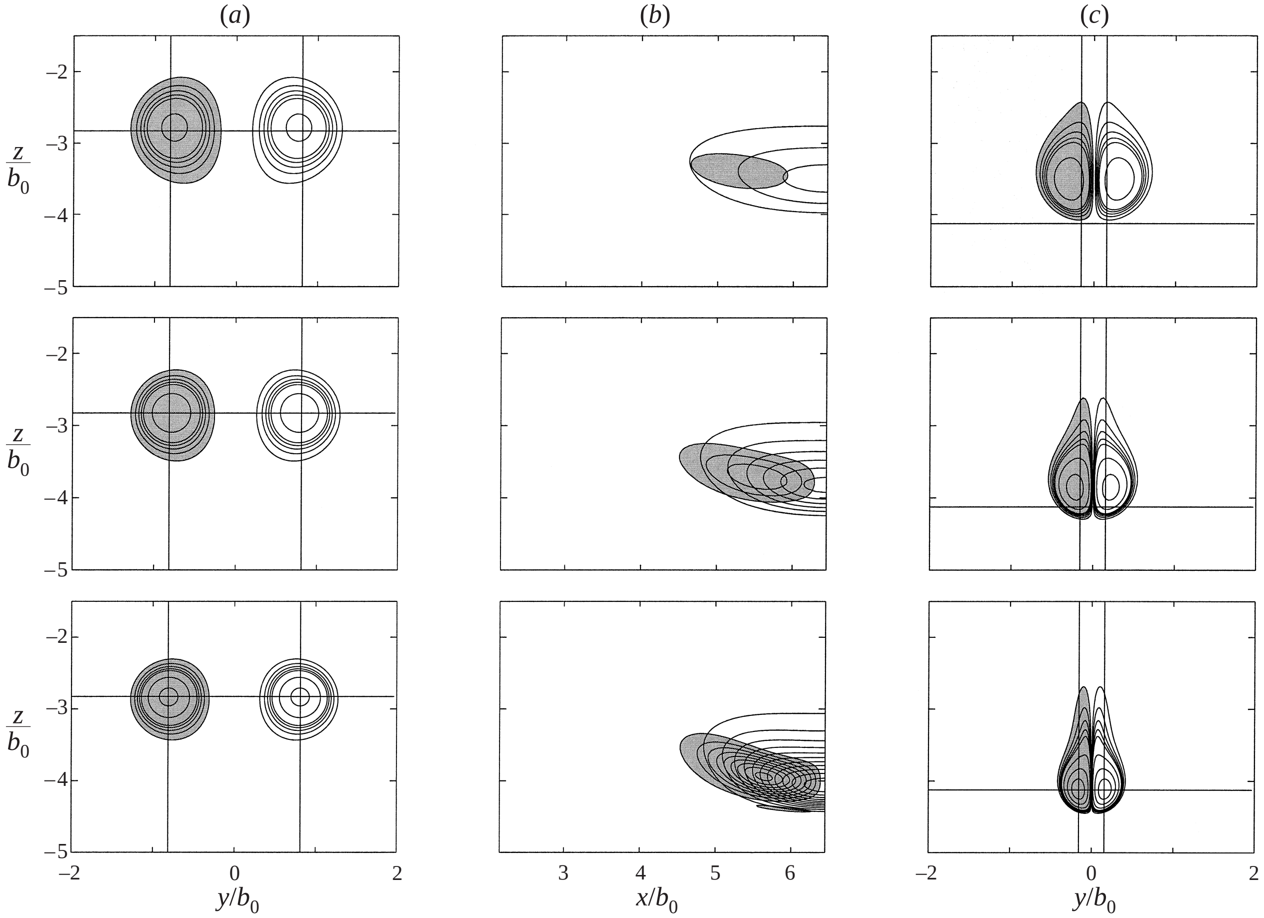

FIGURE 9. As in figure 8, but at $t = 3.5$, and now the middle row shows the $Re = 942$ case, while the column (*b*) contains contours of $(2\pi/Re)(\partial\omega_x/\partial y)$ (showing the magnitude and distribution of cross-diffusion) and $(2\pi/Re)(\partial^2\omega_y/\partial y^2)$ (showing the magnitude and distribution of reconnecting vorticity) in the centreplane between the positions of furthest separation and closest approach of the vortex tubes. Contours of $(2\pi/Re)(\partial\omega_x/\partial y)$ are shown at $-0.25, -0.5, -0.75$, etc., while contours of $(2\pi/Re)(\partial^2\omega_y/\partial y^2)$ are shown at $-0.5, -1.0, -1.5$, etc., and all regions enclosed by contours of $(2\pi/Re)(\partial^2\omega_y/\partial y^2)$ are shaded.

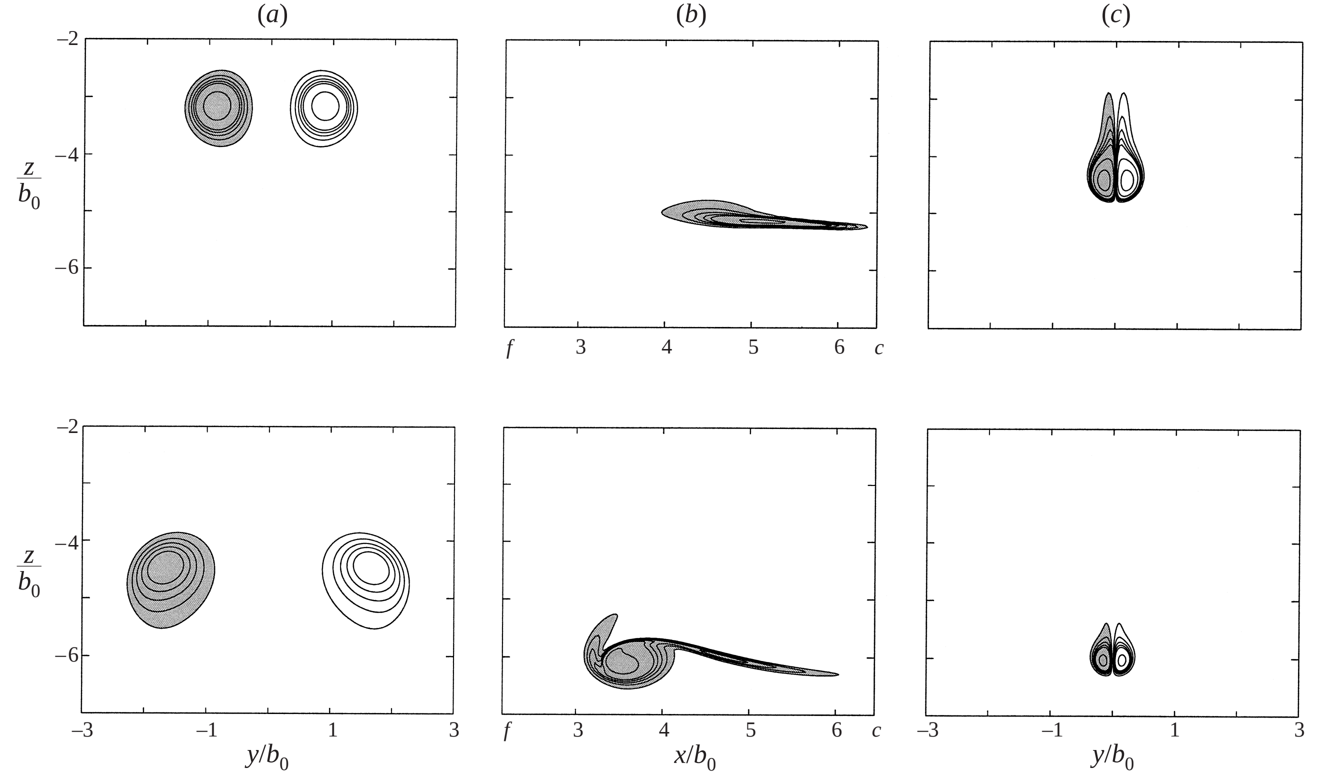

FIGURE 10. As in figure 8, but for the case $Re = 942$ at the times $t = 4$ (top) and $t = 6.25$ (bottom), and now the column (*b*) shows the contours of spanwise vorticity (ω_y) in the centreplane between the vortices, from the positions of furthest separation and closest approach of the vortex tubes.

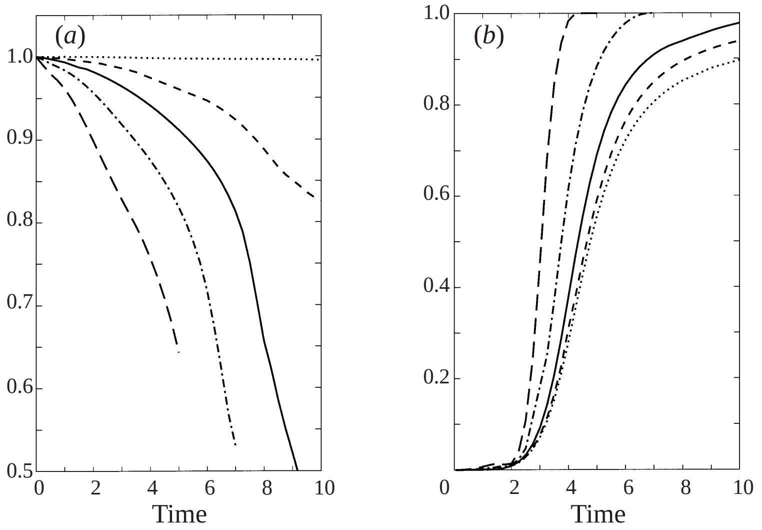

FIGURE 11. The time evolution of the undisturbed circulation of each vortex tube ($\Gamma_f/\Gamma_0, a$) and the fraction of circulation that is reconnected into a vortex ring ($\Gamma_r/\Gamma_f, b$) for the $Re = 942$ cases with $Fr = \infty$ (dotted), $Fr = 8$ (short-dashed), $Fr = 4$ (solid), $Fr = 2$ (dot-dashed), and $Fr = 1$ (long-dashed).

fourth terms of (4.2)) at the same time that the limit on cross-diffusion elongates the vortex cores in the vertical direction (see, e.g. Melander & Hussain 1989). The early stages of this deformation can be seen in figure 8, but it becomes more apparent at the later times shown in figure 9 and figure 10.

The apparent convergence of the instability growth towards the classical Crow prediction (see figure 3), coupled with the head–tail deformation of the vortex tubes, may suggest that a vortex reconnection timescale (t_R) should have straightforward dependence on or even become independent of *Re* in the limit of large *Re*. The rate of reconnection is governed by the integral over the centreplane of the products of $1/Re$ with vorticity gradients at the centreplane as shown by (4.2) and (4.4). It is possible that the increase in deformation with increasing *Re* (see figure 9, and also Kida *et al.* 1991*b*) could increase the vorticity gradients over a larger area in such a way that the time dependence of the area integral would possess a straightforward dependence on *Re*. How t_R depends on both *Re* and *Fr* is discussed more fully in § 4.3.

We next consider why, as can be observed from figures 1 and 7, the vortex tubes do not actually attain complete reconnection. This is an extremely important issue to understand for (at least) two reasons: the better we understand what process(es) prevents complete reconnection within the *Re* range we consider, the better we can predict confidently that reconnection would be incomplete for larger *Re* than we have accessed, and also, the better we can test and predict how external effects (e.g. stratification) may interfere with this process. We now summarize Melander & Hussain's (1989) conceptual reconnection model, and follow in § 4.4 with specific comparisons to our results. Melander & Hussain called the parts of the vortex tubes which do not reconnect 'threads', and argued that their later time evolution is controlled largely by the vortex bridges. The bridges initially possess a curved shape and so move away from one another under self-induction (see their figure 2), while the flow they induce in the centreplane decreases the curvature of the threads. The curvature of the threads is important because (when the threads curve towards one another at their point of closest approach) it leads to self-induction of each thread closer to the centreplane†, subsequently larger vorticity gradients at the centreplane, and thus more rapid reconnection. According to their results, the curvature of the threads eventually reverses, and self-induction then leads to an increase in thread separation, and thus to a near halt in further reconnection. Melander & Hussain also note that the flow induced by the bridges stretches the threads; this effect increases vorticity gradients at the centreplane, and so the reconnection proceeds at a rate slightly faster than if the curvature of the threads were the sole concern.

Our interpretation of Melander & Hussain's conceptual model is that curvature reversal of the threads by the bridge flow field is a process which prevents complete reconnection. However, we believe it may not be the only such process. In support of this belief, we note that in our simulations, the threads begin to move apart from one another (see figure 20*a*) even though their curvature never reverses (see figure 19*a*). This is a very complex and potentially controversial point, and we discuss our interpretation in great detail in § 4.4.

To conclude our discussion of the vortex reconnection phase for the unstratified cases, we consider Melander & Hussain's comment that the threads could eventually undergo a secondary instability and reconnection process themselves as part of a cascade mechanism (involving recursive reconnection events of thread remnants) to smaller scales. In our $Re = 942$ and $Re = 1260$ cases, a point is reached at which the thread separation at plane c is no longer the minimum thread separation (see the definition of κ_y in § 4.4 and its reversal in sign in figure 19*b*). This could be because the process which leads to thread separation decreases in importance away from plane c, but a detailed analysis of this point lies beyond our present means. These new perturbations lead to what could be called secondary reconnection events, centred at two positions along the threads (symmetric with respect to plane c).

We believe that our limited range of Re prevents us from observing this secondary reconnection in all its potential splendour. Even though the $Re = 942$ case was extended to $t = 12$ (past which the solution is impacted intolerably by the computational domain boundaries), the secondary reconnection only reaches an amplitude of roughly 4%. We believe that the secondary reconnection plateaus by $t = 8$ for the $Re = 1260$ case at roughly 12%, but computational expense prevents us from computing further. We can, however, augment these results with two larger Re runs (also used in § 4.3) which utilize the filtering technique described in § 2.3. Insofar as we believe these results, they indicate that secondary reconnection plateaus at roughly 30% and 50% by roughly $t = 7$ and $t = 6$ for $Re = 2200$ and $Re = 3140$, respectively. These solutions also suggest that the positions of secondary reconnection are closer to the bridge locations (and thus further away from the first reconnection position) for larger Re. However, the poor quality of these solutions prevents us from drawing too many inferences, and we believe they should be used to guide, not replace, future direct simulations with larger Re.

4.2. *Vortex reconnection in a stratified fluid*

We now consider how ambient stratification affects the vortex reconnection phase of the evolution. The timescale analysis in § 3.2 suggests the evolution should not change for large Fr. However, the vortex reconnection phase should be affected more than

---

† Only in the case that the threads curve towards their point of closest approach but possess constant horizontal positions would the self-induction be *directly* towards the centreplane.

the Crow instability phase for the same *Fr* because its duration is roughly twice as long.

Using the same definitions as before, the time evolutions of Γ_f/Γ_0 and Γ_r/Γ_f are shown in figure 11 for some† of the same *Fr* cases discussed in § 3.2 . The sharp decrease in Γ_f for these stratified cases, when there is virtually no change for the unstratified ($Fr \to \infty$) case, is quite intriguing. The importance of this issue lies in whether or not it supports a PD view of the evolution (Spalart 1998), in which it could be assumed that the circulation gradually changes in some predictable way. This is not the case, as we have determined that the loss in circulation arises from viscous interaction between the primary vortices and baroclinically produced vorticity, and this loss would not be as rapid for larger *Re*. We now elaborate more fully these points.

We focus our attention on the $Fr = 2$ and $Fr = 1$ cases. Contours of the density in planes *f* and *c* for the $Fr = 1$ case are shown in figure 12. These images illustrate the resemblances to the flows of two-dimensional vortex pairs in ambient stratification (see, e.g. Spalart 1996; Garten 1997; and Garten *et al.* 1998). Apart from the diffusive effects in (2.7), the density is a conserved scalar of the flow, and its contours provide a sense of the flow's history. In particular, they show that relatively lighter fluid has been entrained by the vortex tubes and carried downwards, and that the distribution is not uniform along the vortex tubes. By $t = 2.5$, the region of fluid carried with the vortex tubes is internally well mixed, but its boundaries have sharp gradients which can cause numerical noise to appear if the resolution is not increased sufficiently. At later times (not shown here), fluid initially displaced downwards rebounds back upwards due to buoyancy, and this happens more quickly for smaller *Fr*.

The torque of the buoyancy force acting on fluid having a horizontal density gradient creates vorticity through the baroclinic production terms given by

$$\frac{\partial \omega_x}{\partial t} = -\frac{1}{Fr^2}\frac{\partial T}{\partial y}, \tag{4.5}$$

$$\frac{\partial \omega_y}{\partial t} = \frac{1}{Fr^2}\frac{\partial T}{\partial x}. \tag{4.6}$$

From the perspective of vorticity dynamics, these terms contain all buoyancy effects, and so the subsequent effects due to baroclinically produced vorticity may alternatively be viewed as being due to buoyancy. Due to the flow's symmetries, only (4.5) contributes in planes *f* and *c*, while in general, vorticity is produced with both $\hat{x}$ and $\hat{y}$ components (presumably, the ratio of the components is such that the regions of baroclinically produced vorticity are oriented roughly parallel to the primary vortex tubes).

Contours of the $\hat{x}$ component of the baroclinic source of vorticity are also shown in figure 12. Since the distribution of density gradients is not uniform along the vortex tubes, neither is the baroclinic source. The magnitude of the baroclinic source for the $Fr = 1$ case is larger than for larger *Fr*. Even though the density gradients are roughly the same (at $t = 2.5$), the source behaves as $1/Fr^2$, and so its magnitude is larger for smaller *Fr*. Though it is difficult to see from the contours shown, the magnitude of the baroclinic source is also larger where the separation distance of the vortex tubes is smaller. This results from the more rapid descent of the vortex tubes where their

---

† In the $Fr = 1/2$ case, the amplitude of the Crow instability does not become large enough to initiate vortex reconnection. Therefore, when we discuss *Fr* dependences of the vortex reconnection in our solutions, we will implicitly mean $Fr \geqslant 1$.

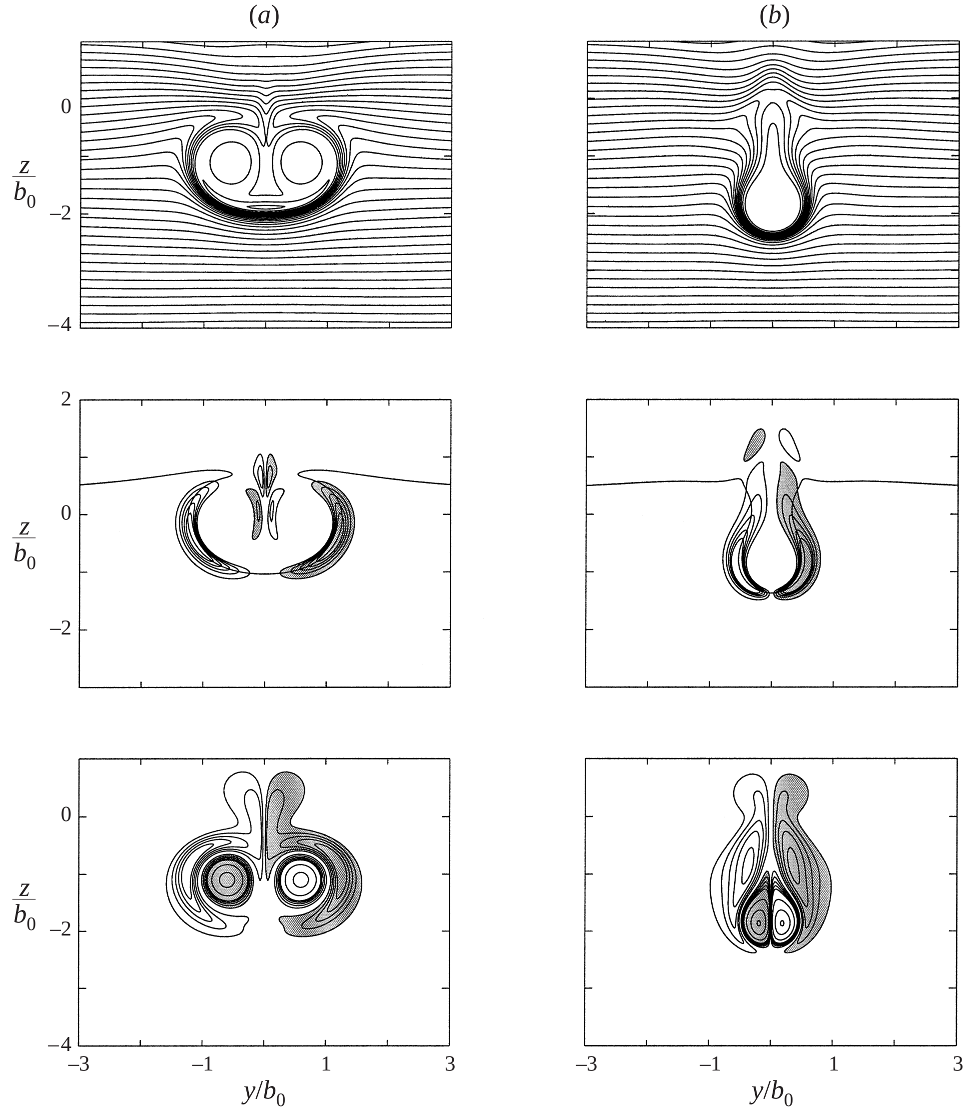

FIGURE 12. Contours of the density (top), the baroclinic source of vorticity (middle), and the vorticity (bottom) in planes f (*a*) and c (*b*) of the vortex tubes for the $Fr = 1$ case at $t = 2.5$. Density contours are at intervals of 0.15, while contours of the baroclinic source and the vorticity are shown at $\pm1, \pm2, \pm3, \pm4, \pm5, \pm10, \pm20, \pm30$, etc. Regions enclosed by negative contours are shaded, and one of the density contours has been drawn over the baroclinic source.

separation distance is smaller, and the subsequent larger density gradient between the background fluid and the fluid carried with the vortex tubes.

Contours of vorticity are also shown in figure 12 and, for the $Fr = 2$ case, in figure 13. Since the baroclinic source is not uniform along the vortex tubes, neither is the distribution of the secondary, baroclinically produced vorticity, which concentrates into sheets to the side of and just behind the primary vortices. As discussed in § 3.2, these secondary regions of countersign vorticity advect the primary vortices towards one another, and decrease their average separation distance (e.g. figure 6). Although this decrease results in the acceleration of a two-dimensional vortex pair (for large

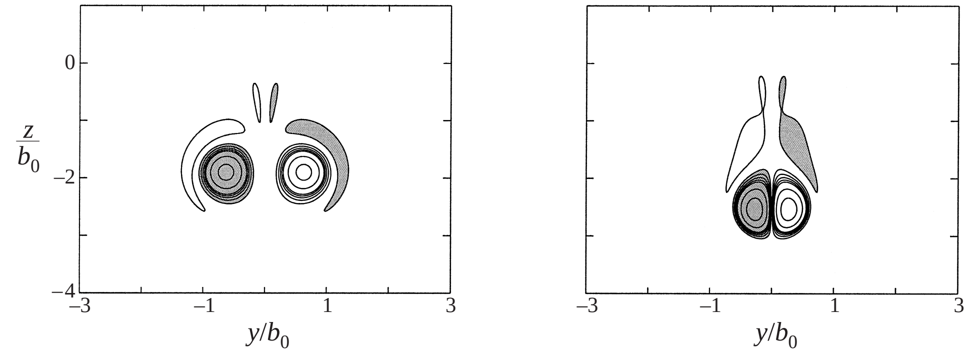

FIGURE 13. As in figure 12 (bottom row) but for the $Fr = 2$ case.

enough Re), it does not lead to an acceleration of these three-dimensional vortex pairs. The acceleration is apparently prevented by the continuous loss in total (and average) circulation of the vortex tubes, though the topological changes (e.g. Γ_c decreases) might also prevent the acceleration even if Γ_f were preserved.

Due to the symmetries of the flow, the continuous loss in Γ_f (compared to the unstratified case) must result from net cancellation with the oppositely signed baroclinic vorticity and/or enhanced cross-diffusion of the primary vortices caused by their advection towards the centreplane by the baroclinic vorticity. Consider the contours of ω_x in the spanwise plane f shown in figure 14 for the $Fr = 2$ case. In this case, *all* regions of negative vorticity have been shaded so that the boundaries of zero vorticity are visible. Until $t \simeq 3.5$, the primary vortices are not in contact with one another in plane f, and so there is zero cross-diffusion between them in plane f. After $t \simeq 3.5$, some cross-diffusion occurs (e.g. between $z \simeq -3.75$ and $z \simeq -2.5$ at $t = 4.5$), but the contours of vorticity suggest visually that the viscous cancellation between each primary vortex and its neighbouring baroclinic vorticity is a much larger contributor to $\partial\Gamma_f/\partial t$. For a quantitative comparison, it can be shown that the instantaneous contribution to $\partial\Gamma_f/\partial t$ by cross-diffusion can be calculated by integrating $-(2\pi/Re)\partial\omega_x/\partial y$ over the portion of the centreline where the primary vortices are in direct contact.

The time evolution of the fraction of $\partial\Gamma_f/\partial t$ due to cross-diffusion for our $Fr \geqslant 1$ cases is shown in figure 15(a), and it clearly indicates that the major contributor to $\mathrm{d}\Gamma_f/\mathrm{d}t$ must be net cancellation with the baroclinic vorticity. With this in mind, we now make indirect comparisons to a set of two-dimensional solutions to determine whether or not we believe Γ_f would decrease as sharply for larger Re. The time evolutions of the circulation of two-dimensional vortex pairs computed at $Fr = 2$ and several Re are shown in figure 15(b). Qualitatively, the circulation in each case decreases initially due to net cancellation with baroclinic vorticity (up to roughly $t \simeq 3-4$), but then decreases more rapidly due to cross-diffusion accelerated by the vortices' advection towards one another by the baroclinic vorticity. This second phase is irrelevant for our desired comparison to the three-dimensional case, as the Crow instability increases the separation distance in plane f and, as already determined, cross-diffusion is never a major contributor to $\partial\Gamma_f/\partial t$. The time evolution of $\partial\Gamma/\partial t$ up to the time (in each case) when cross-diffusion begins to contribute more than 10% for the two-dimensional cases is shown in figure 15(c). Clearly, the circulation decreases more slowly for larger Re, and we infer for the general (laminar) three-dimensional case that Γ_f would decrease more slowly (for fixed Fr) for larger Re.

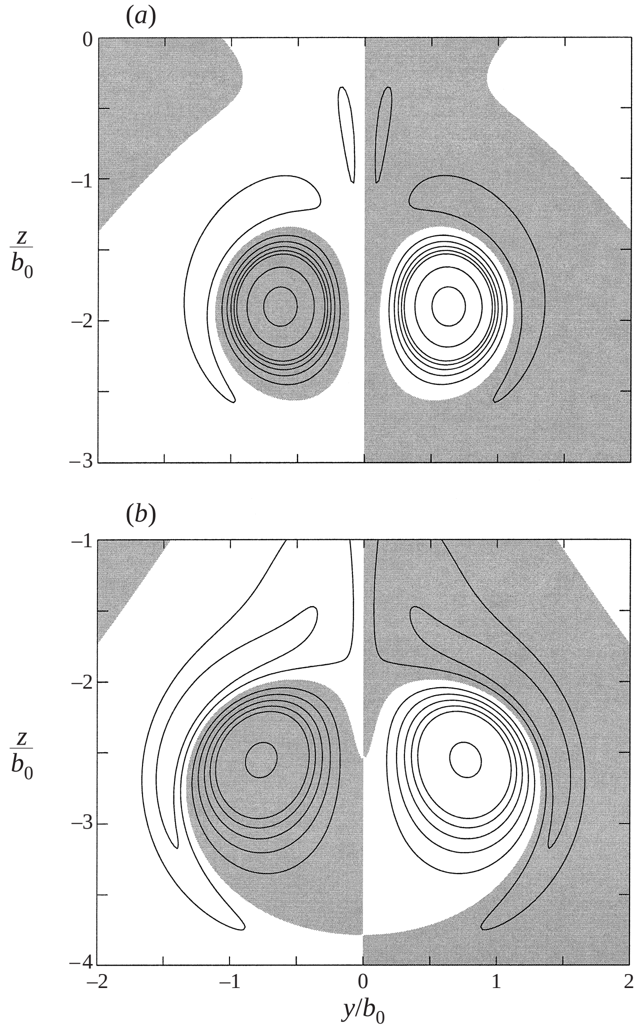

FIGURE 14. Contours of the vorticity in plane f for the $Fr = 2$ case at (a) $t = 2.5$ and (b) $t = 4.5$. The contour levels are shown at $\pm1, \pm2, \pm3, \pm4, \pm5, \pm10, \pm20, \pm30$, etc., and all regions of negative vorticity have been shaded.

Now consider the time evolution of Γ_r/Γ_f (see figure 11). We note that in terms of net production of spanwise circulation *on the centreplane*, (4.2) is supplemented by (4.6) for the stratified cases. Baroclinically produced vorticity augments the ring vorticity, and so the minimum circulation of the vortex ring is no longer exactly $\Gamma_f - \Gamma_c$. However, we have determined that the total contribution of the baroclinic term is less than 5% of the contribution by reconnection (i.e. the source part of the first term of (4.2)). Therefore, we continue to use $\Gamma_f - \Gamma_c$ as an approximate measure of the minimum circulation of the vortex ring. Because Γ_f/Γ_0 decreases so sharply, the quantity Γ_r/Γ_0 gives a better estimation of the minimum circulation (the maximum circulation is Γ_f/Γ_0) of the vortex ring as it forms (see figure 16). Through consideration of either of these quantities, it is clear that the reconnection proceeds more rapidly for smaller Fr. In fact, for the $Fr \leqslant 2$ cases, the reconnection also reaches completeness (see figure 11) in the sense that no original vorticity survives in

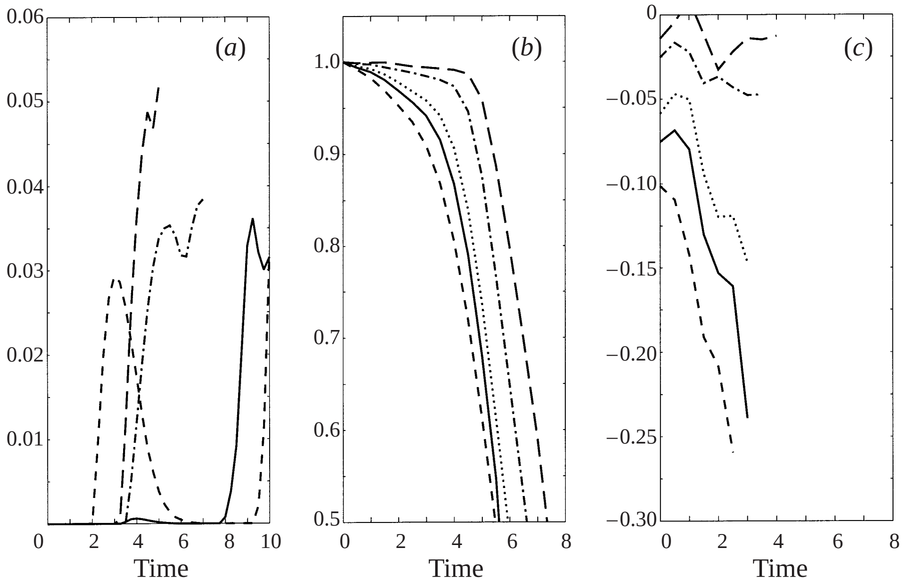

FIGURE 15. (*a*) The fraction of $\mathrm{d}\Gamma_f/\mathrm{d}t$ that is due to cross-diffusion of the primary vortices for the $Re = 942$ cases with $Fr = 8$ (short-dashed), $Fr = 4$ (solid), $Fr = 2$ (dot-dashed), and $Fr = 1$ (long-dashed). (*b*) The time evolution of the circulation of two-dimensional vortex pairs with $Fr = 2$ and $Re = 942$ (short-dashed), $Re = 1260$ (solid), $Re = 1570$ (dotted), $Re = 3140$ (dot-dashed), and $Re = 6280$ (long-dashed). (*c*) $\mathrm{d}\Gamma/\mathrm{d}t$ upto the time (in each case) at which cross-diffusion begins to contribute more than 10% to the total for the same cases shown in (*b*).

plane c and there are no threads of vorticity that survive external to the vortex ring as in the larger Fr cases. This occurs by $t \simeq 7$ and $t \simeq 5$ for the $Fr = 2$ and $Fr = 1$ cases, respectively. The reasons for this sharp departure from the unstratified result of incomplete reconnection no matter how rapidly it proceeds at intermediate times are discussed in § 4.4.

The faster reconnection in the stratified cases results from the advection of the primary vortices toward the centreplane by the baroclinic vorticity (already discussed). Although this advection is not present in (4.2)–(4.4) (as augmented by (4.6)), its effects are felt through the steepening of the vorticity gradients that are present in the centreplane equations. Contours of $(2\pi/Re)(\partial\omega_x/\partial y)$ (showing the magnitude and distribution of cross-diffusion) and the source part of $(2\pi/Re)(\partial^2\omega_y/\partial y^2)$ (showing the magnitude and distribution of actual reconnection of vorticity) are shown in figure 17. These contours indicate clearly that the vorticity gradients increase more rapidly (in both magnitude and extent) for smaller Fr, and so the reconnection proceeds more rapidly. We note that, although it is not shown in figure 17, cross-diffusion of baroclinically produced vorticity also occurs (in the stratified cases) at the centreplane in the regions where the baroclinic sheets of vorticity are detrained behind the primary vortices (see, e.g. the $Fr = 1$ case at $t = 2.5$ in figure 13). The baroclinic vorticity has the opposite sign of the original vorticity, and so its contributions to $(2\pi/Re)(\partial\omega_x/\partial y)$ and $(2\pi/Re)(\partial^2\omega_y/\partial y^2)$ are of the opposite sign as well.

We note that Virk *et al.* (1995) found that compressible effects (specifically, shocklet-aided bridging) also lead to faster reconnection. However, that effect then leads to a longer reconnection timescale as the earlier circulation transfer impedes growth in curvature of the vortex tubes, and the curvature reversal effect then occurs more

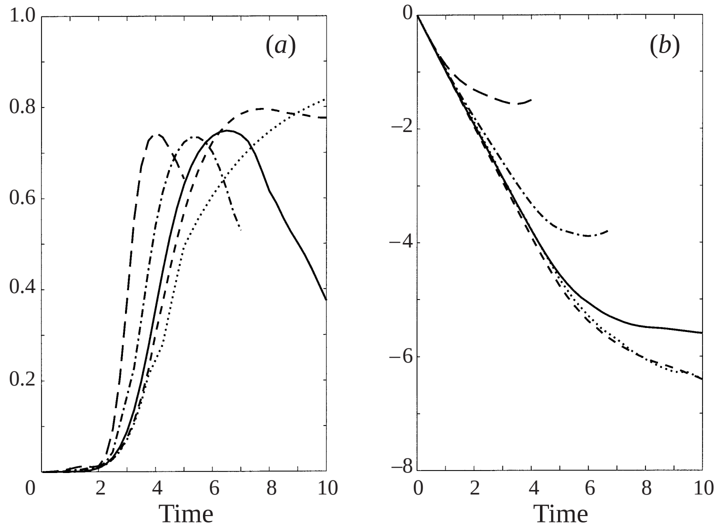

FIGURE 16. The time evolution of Γ_r/Γ_0 (*a*) and the average vertical position of the primary vorticity (*b*) for the $Re = 942$ cases with $Fr = \infty$ (dotted), $Fr = 8$ (short-dashed), $Fr = 4$ (solid), $Fr = 2$ (dot-dashed), and $Fr = 1$ (long-dashed).

rapidly. This effect is quite different from the (incompressible) stratification effect we have discussed, whereby circulation transfer is enhanced at all times via the decrease in $\langle b \rangle$ caused by the baroclinic vorticity. If we understand their results correctly, they used a constant $Fr \simeq 2.2$ for all of their calculations, and varied the speed of sound to vary their Mach number M. We believe that if Fr were varied for fixed M, then the reconnection timescale would decrease for smaller Fr (within the nonlinear regime of Fr).

Consider the possible discrepancy between our results and the results of Virk *et al.*: reconnection is increased at all times (see figure 11) in our stratified flows (the $Fr = 2$ case gives the closest comparison to Virk *et al.*'s $Fr = 2.2$) via advection by baroclinic vorticity towards the centreplane, while reconnection is increased slightly at early times but decreased slightly at later times in Virk *et al.*'s stratified and compressible $M = 0.5$ flow (compared to their incompressible, unstratified flow – see their figure 5*a*). Why is the evolution of their $M = 0.5$ case, stated to be largely incompressible (though still stratified), not more consistent with the evolution of our stratified flows? One must make this comparison between the flows very carefully.

We believe it is clear from Virk *et al.*'s figure 2(*a*) that their threads undergo curvature reversal well before $t = 6$ and perhaps as early as $t = 4.1$. As stated previously, self-induction of each thread then contributes to an increase in thread separation (presumably overriding the contribution to a decrease in thread separation by the baroclinic vorticity) and a decrease in reconnection. This is borne out by Virk *et al.*'s figure 12(*a*) which shows that thread separation begins to increase at roughly $t = 4.5$. In all of our flows, however, the curvature of the threads never reverses and, in our $Fr = 2$ and $Fr = 1$ cases, thread separation decreases at all times (see figure 20*c*). We believe that the curvature reversal, or lack thereof, is a key difference between the flows, and believe it occurs in Virk *et al.*'s $M = 0.5$ case but not our flows for (at least) the following two reasons: first, their larger initial perturbation appears to lead more easily to curvature reversal (this point is discussed within the comparisons

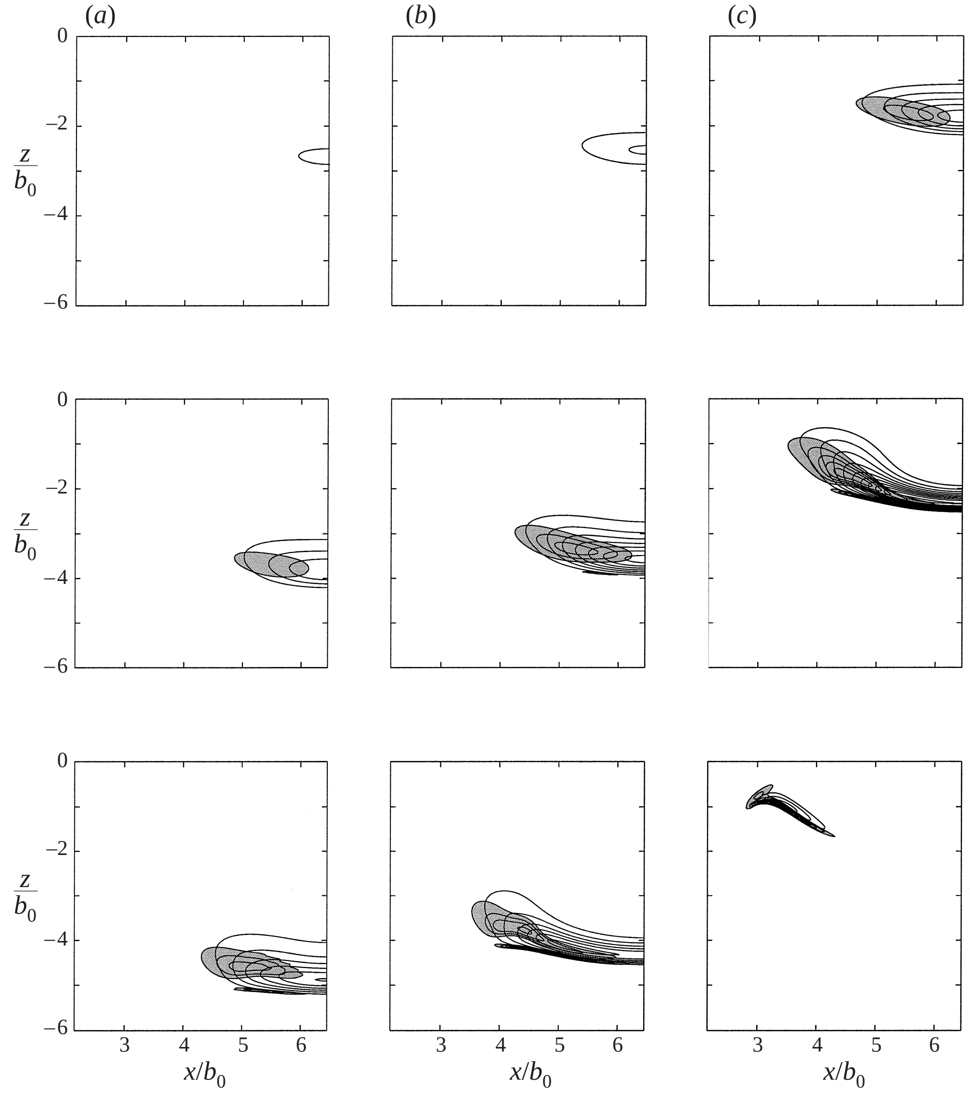

FIGURE 17. Contours of $(2\pi/Re)(\partial\omega_x/\partial y)$ (showing the magnitude and distribution of cross-diffusion) and $(2\pi/Re)(\partial^2\omega_y/\partial y^2)$ (showing the magnitude and distribution of reconnecting vorticity) in the centreplane between the positions of furthest separation and closest approach of the vortex tubes for the $Re = 942$ cases with $Fr = \infty$ (*a*), $Fr = 2$ (*b*), and $Fr = 1$ (*c*) at $t = 2.5$ (top), $t = 3.5$ (middle), and $t = 4.5$ (bottom). Contours of $(2\pi/Re)(\partial\omega_x/\partial y)$ are shown at $-0.4, -0.8, -1.2$, etc., while contours of $(2\pi/Re)(\partial^2\omega_y/\partial y^2)$ are shown at $-1.0, -2.0, -3.0$, etc., and all regions enclosed by contours of $(2\pi/Re)(\partial^2\omega_y/\partial y^2)$ are shaded.

made in §4.4); and second, even if the $M = 0.5$ case is largely incompressible, the compressible effect still slightly increases the reconnection at early times (the pattern of behaviour in their figure 5(*a*) seems obvious), and, as Virk *et al.* discuss, this earlier reconnection leads to even more rapid curvature reversal.

Finally, the contours shown in figure 17 indicate that the primary vorticity propagates downwards less far for smaller *Fr* (e.g. in the $Fr = 1$ case, all of the reconnection occurs at a height that is nearly constant when compared to the unstratified case).

The time evolution of the average vertical position of the primary vorticity is shown in figure 16(*b*) for all of our stratified cases; in each case, this average position is only tracked while the primary vortices can be viewed as the dominant flow feature. These plots confirm that a smaller *Fr* results in the primary vortex ring not penetrating as far down, and in fact propagating back upwards slightly while it remains the dominant flow feature. The slowed descent of the primary vortices apparently results from the decrease in their total circulation (see figure 11), while the tendency to propagate back upwards results from the flow field of the baroclinic vorticity.

4.3. *Vortex reconnection timescale dependences*

The curves in figures 7, 11, and 16, indicate that reconnection occurs on a faster timescale for larger *Re* and smaller *Fr* (within the ranges we have considered); we now discuss a reconnection timescale (t_R) that captures these dependences. To remove arbitrariness potentially brought about by our specific choice of initial conditions, and to avoid decisions on when the reconnection begins or concludes, we measure t_R in the following way: we define t_R as the negative inverse of $\partial\Gamma_c/\partial t$ at the instant in time when $\Gamma_c = \Gamma_f/2$. Note that t_R is the time it would take for complete reconnection were $\partial\Gamma_c/\partial t$ constant for all time.

Shelley *et al.* (1993) summarized the theories of Siggia & Pumir (1987) on singularity configurations and extended their results to predict $t_R \sim 1/Re$ (for our definition of t_R) for the unstratified case. They also summarized work by Kambe (1983) and Buntine & Pullin (1989) which leads to predictions that t_R has logarithmic dependence on *Re* for large *Re*. However, our results agree quite well with the extension to Siggia & Pumir's work, and we therefore include only a summary of that theory and attempt to extend it to the stratified case.

Following Shelley *et al.* (1993), the decay of the circulation (Γ) and change in the separation distance (δ) can be crudely modelled by

$$\frac{\partial\Gamma}{\partial t} = -\frac{1}{Re}\frac{\Gamma}{\delta^2}, \tag{4.7}$$

$$\frac{\partial}{\partial t}\delta^2 = -\Gamma, \tag{4.8}$$

and these equations can be combined to obtain

$$\delta^2(t) = \mathrm{e}^{Re(\Gamma(t)-1)}, \tag{4.9}$$

where the initial separation and circulation are taken to be 1. The circulation remains virtually constant until the singularity time, given by $t_s = 1$ in these units, and then drops rapidly to zero over a time equal to t_R. It is then possible to show via asymptotic expansion that for large $Re\, t_R \sim 1/Re$.

The values of t_R as measured from our three unstratified simulations are shown in figure 18(*a*). Because of our limited range of *Re*, we have decided to augment these results with the results of two larger *Re* runs which utilize the filtering technique described in §2.3. A least-squares fit of these five data points to the functional form c_r/Re yields $c_r \simeq 4200$, and the curve corresponding to $4200/Re$ is also shown in figure 18(*a*) for comparison. As previously intimated, our results appear to agree quite well with the prediction of this model. It is interesting to note that inclusion of the two larger *Re* measurements changes c_r by less than 0.5%.

Now, consider how to extend this model to the stratified case. One approach is to simply include another term in (4.8) that accounts for the advection of the vortices by the baroclinic vorticity. Because time is normalized by the singularity time in this

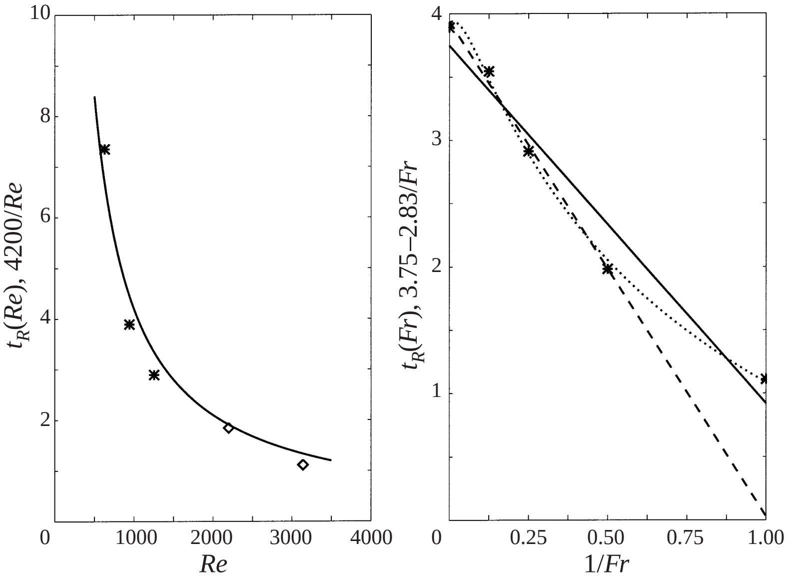

FIGURE 18. (*a*)The values of t_R as a function of *Re* for our resolved (star symbol) and filtered (diamond symbol) unstratified simulations, compared to the curve 4200/*Re*. (*b*) The values of t_R as a function of *Fr* (star symbol) for our stratified simulations (all at $Re = 942$), compared to the curves $3.75 - 2.83/Fr$ (solid), $3.94 - 3.91/Fr$ (dashed), and $3.94 - 7.76\exp(-\sqrt{Fr})$ (dotted).

model, however, it would be quite problematic to include a time-dependent term. As already discussed, the results of previous two-dimensional numerical simulations as well as the three-dimensional numerical simulations reported here indicate that the advection by the baroclinic vorticity decreases the separation distance in general accordance with $b \sim \exp(-c_0 t/Fr)$ for some constant c_0 (see Spalart 1996, the discussion of equation (3.7) and figure 6 in Garten *et al.* 1998, and figure 6 of this paper). The leading-order approximation to the contribution of the advection by the baroclinic vorticity to $\partial b^2/\partial t$ is then $-2c_0/Fr$, and we believe that (4.8) is then best modified as follows:

$$\frac{\partial}{\partial t}\delta^2 = -\Gamma - \frac{c}{Fr}, \tag{4.10}$$

where we relax preconceptions regarding the value of the constant c. Equation (4.9) then becomes

$$\delta^2(t) = \Gamma^{cRe/Fr} e^{Re(\Gamma(t)-1)}, \tag{4.11}$$

and it is possible to show that $t_R \sim 1/Re - c/Fr$.

The measured values of t_R for our stratified cases are shown in figure 18(*b*), plotted against $1/Fr$ so that the unstratified ($Fr \rightarrow \infty$) case may be included. A least-squares fit of these five data points to the functional form a–c/Fr[†] yields $a = 3.75$ and $c = 2.83$, and the curve corresponding to $3.75 - 2.83/Fr$ is shown in figure 18(*b*) for comparison. In this case, the agreement between our data and the model's prediction is not as good. However, if we exclude the $Fr = 1$ result from the least-squares fit, we obtain $a = 3.94$ and $c = 3.91$, and the agreement improves substantially (see figure

---

[†] Since all of the stratified cases are at the same *Re*, we believe it is best to calculate the least-squares fit for $t_R(Fr)$ independently of the previous one that found $c_r = 4200$, or equivalently, $a = 4.46$.

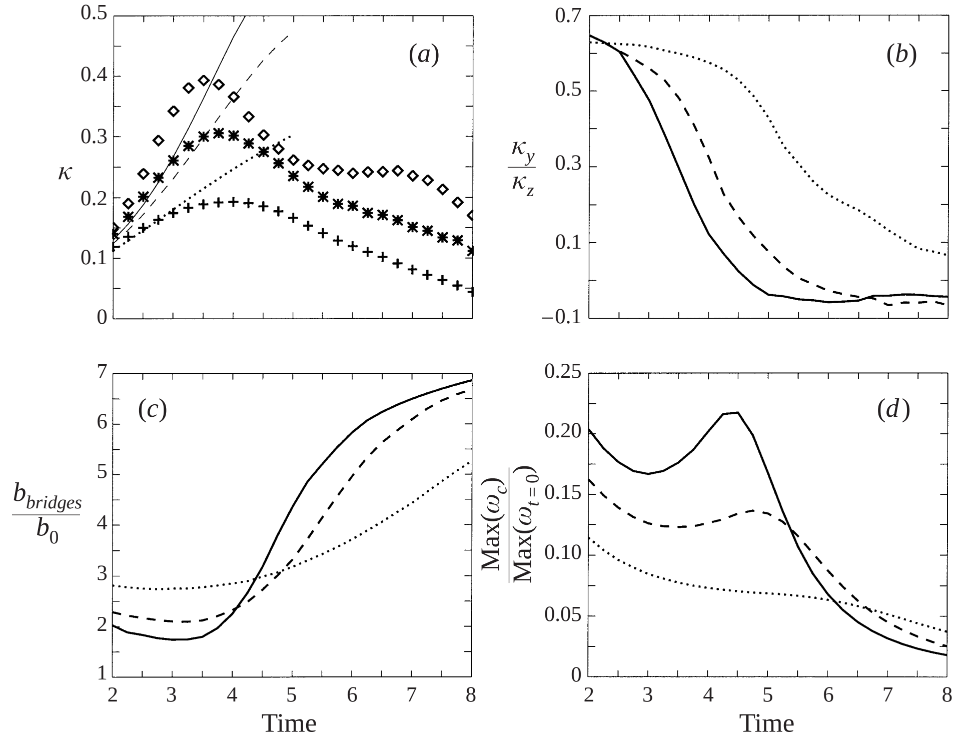

FIGURE 19. (*a*) The absolute curvature κ of the vortex tubes at plane *c* (plotting symbols), compared to the expected κ from instability growth alone (lines), for the unstratified cases with $Re = 628$ (cross, dotted), $Re = 942$ (star, dashed) and $Re = 1260$ (diamond, solid). (*b*) As in (*a*), but now lines shows the actual curvature ratio (κ_y/κ_z). (*c*) As in (*b*), but for the separation distance between the vortex bridge centroids. (*d*) As in (*b*), but for the maximum value of vorticity in plane *c*.

18*b*). In anticipation of models that may arise to predict different functional forms for $t_R(Fr)$, we also note that a survey of polynomials and exponential functions shows that the function $3.94 - 7.76 \exp(-\sqrt{Fr})$ fits our data quite well (see figure 18*b*).

4.4. *On the completeness of reconnection*

We begin our comparisons to Melander & Hussain's conceptual model with figure 19(*a*), which shows the time evolution of the absolute curvature, κ, of the vortex tubes at their position of closest approach (plotting symbols). At early times, the curvature increases because of instability growth: in the absence of other effects, the curvature of a sinusoidal displacement is proportional to its amplitude. However, κ increases more than would be expected from the instability growth alone (line plots), and the discrepancy increases for larger *Re*. We believe that the positive feedback between self-induction closer to the centreplane due to increased curvature and faster propagation of the closest portion of the vortex tubes (see, e.g., Moore 1972; Saffman 1992) is responsible for this discrepancy, and we expect that the peak value of κ continues to increase for still larger *Re*. However, we note that the time at which the peak κ is attained decreases with time (towards some non-zero limit), and this suggests that other effects do intervene to keep κ from racing off to ∞.

We first point out that the positive feedback mechanism that increases curvature relies on the assumption of constant circulation with time (as well as on assumptions regarding core distribution, of which we do not attempt inclusion), but of course the thread circulation at the position of closest approach (Γ_c) decreases with time. However, there does not appear to be a clear connection between Γ_c at the time of peak κ for the different *Re* cases. The time of peak κ is roughly $t = 4$, 3.8, and 3.5 for $Re = 628$, 942, and 1260, respectively, while $\Gamma_c/\Gamma(0)$ for each case and given time is roughly 0.77, 0.76, and 0.82. Therefore, we next look for evidence that flow induced by the vortex bridges is responsible more directly for the decrease in curvature (as explained by Melander & Hussain).

Figures 1 and 10 give a visual sense of the location of the vortex bridges with time for the $Re = 942$ case, while figure 19(*c*) shows the time evolution of the horizontal distance between the centroids of the two vortex bridges where they intersect the centreplane for all three cases. Since bridge formation is a continuous process, it is difficult to pick a particular time to look for subsequent effects on the thread curvature. However, it is reasonable to assume that once bridge circulation builds up significantly, the self-induction of each bridge away from the other should be virtually simultaneous with their induced flow's decrease in curvature of the threads. In fact, our results show that the time at which the two vortex bridges begin to move quickly apart from one another (figure 19*c*) is in each case consistent with the time of peak κ (a point of strong agreement with Melander & Hussain).

Melander & Hussain also predicted that stretching of the threads by the vortex bridges sustains reconnection and also ensures well-defined vortex cores. Figure 19(*d*) shows the peak magnitude of vorticity in plane c, ω_c (i.e. $\omega_c = \mathrm{Max}\,(\omega_x(x = c, y, z))$), normalized by the value at $t = 0$. At early times ($t \leqslant 2.5$), ω_c decreases because of viscous expansion. This is because viscous expansion leads to a larger vortex core size (e.g. (3.1)), and, for constant circulation, the product $\sigma^2\omega_c$ remains constant (for Gaussian vortices, $\Gamma = 2\pi\sigma^2\omega_c$). Once reconnection commences, the circulation decreases, and, if we neglect the core deformations from the Gaussian distribution, ω_c decreases further. However, our results show that ω_c does increase after a time, again consistent with significant bridge formation (though slightly earlier in each case than the time suggested by the curvature and separation effects). Although this is another point of agreement with Melander & Hussain, we note that this stretching-induced increase in ω_c is not sustained, as Melander & Hussain appeared to suggest. We note that the time that the local peak of ω_c is attained is consistent with the time at which the bridge separation is roughly 3.25 for the different *Re* cases (an earlier time for larger *Re*), and that ω_c decreases sharply after this time. Our interpretation is that the stretching effects at the position of closest approach decrease in importance significantly as the spatial distance to the vortex bridges increases. This is an important point in the light of the difference from Melander & Hussain that we discuss next.

We first introduce the following notation. Let κ_y and κ_z represent the curvature of each thread (in magnitude) measured at the position of closest approach when the spatial positions of the thread are projected onto (x, y)- and (x, z)-planes, respectively. The sign of κ_y/κ_z is defined such that $\kappa_y/\kappa_z > 0$ results in self-induction of the positive thread upwards/towards the centreplane, while $\kappa_y/\kappa_z < 0$ results in self-induction of the positive thread downwards/away from the centreplane. As discussed previously, the flow induced by the vortex bridges decreases κ_z (i.e. the curvature is reduced). According to Melander & Hussain, that flow then changes the sign of κ_z (i.e. the curvature is reversed), and the threads self-induct away from one another, effectively arresting the reconnection. Although this curvature reversal occurs fairly rapidly in their results (see their figure 2), we cannot stress enough that κ_z does not change sign

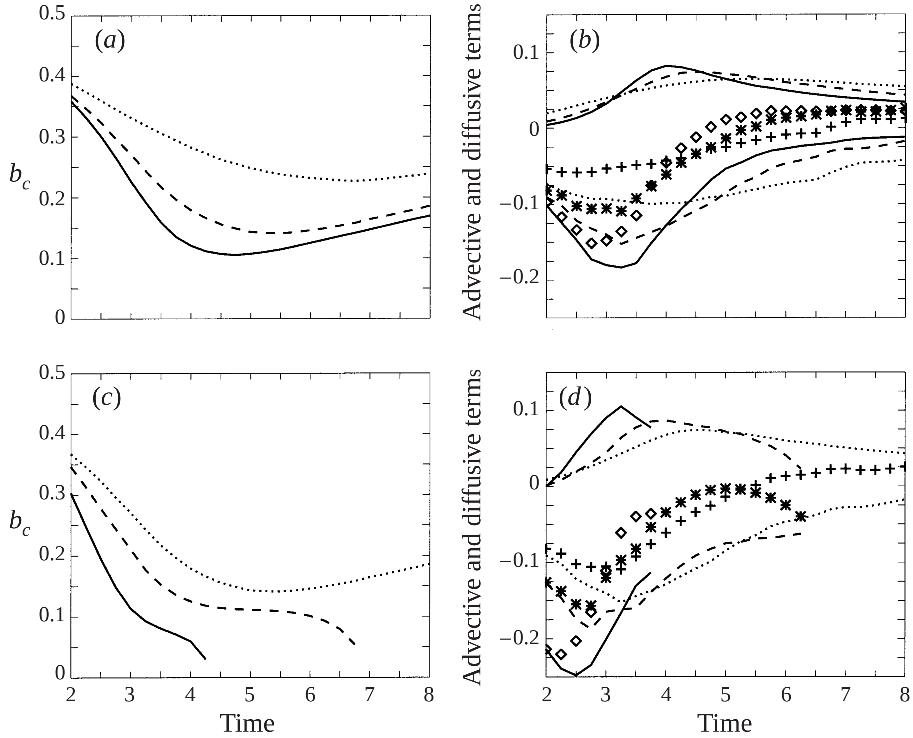

FIGURE 20. (*a*) As in figure 19, but for y_c. (*b*) As in figure 19, but for the total advective (three lower curves) and diffusive (three upper curves) contributions to $\partial y_c/\partial t$, as well as their total (plotting symbols). (*c*) As in (*a*), but for the $Re = 942$ cases with $Fr = \infty$ (dotted), $Fr = 2$ (short-dashed), and $Fr = 1$ (solid). (*d*) As in (*b*), but for the $Re = 942$ cases with $Fr = \infty$ (dotted), $Fr = 2$ (short-dashed), and $Fr = 1$ (solid).

in any of our cases, nor does there appear to be any indication that it would were we to compute our solutions to later times (the $Re = 942$ case has been checked up to $t = 10$, and the $Re = 628$ case has been checked up to $t = 11$). This could be because our smaller initial perturbations may allow the curvature to grow to a much larger peak value (a comparison of our figure 1 and Melander & Hussain's figure 2 does indicate the curvature of our threads is more pronounced), and subsequent advective effects are not strong or persistent enough to completely reverse the curvature. We are not aware of other results that have included explicit quantitative information regarding the time evolution of the curvature, and so have no concrete basis for comparison on this point.

With this important difference in mind, we now point out the both unexpected and quite important observation that the separation distance of our threads at the position of closest approach does increase after roughly $t = 6.75$, 5.5, and 4.75 in the $Re = 628$, 942, and 1260 cases, respectively (see figure 20*a*). This increase is unexpected because so long as $\kappa_z > 0$, the threads should self-induct towards the centreplane, not away from it; it is important because it suggests the possibility of another effect which decreases the rate of reconnection (via decreased vorticity gradients at the centreplane, as for the curvature reversal effect).

To understand how this could occur, we define (y_c, z_c) as the coordinates of the centroid of the positive thread in plane c; specifically†

$$y_c(t) = \frac{\displaystyle\int_0^{L_y/2}\int_0^{L_z} y\omega_x(x=c,y,z,t)\mathrm{d}y\,\mathrm{d}z}{\displaystyle\int_0^{L_y/2}\int_0^{L_z} \omega_x(x=c,y,z,t)\mathrm{d}y\,\mathrm{d}z}, \tag{4.12}$$

where the denominator is equal to the circulation $\Gamma_c(t)$. The time rate of change of y_c can be computed straightforwardly, and rearranged into the form

$$\frac{\partial y_c(t)}{\partial t} = \frac{1}{\Gamma_c(t)}\int_0^{L_y/2}\int_0^{L_z}(y-y_c(t))\left.\frac{\partial \omega_x}{\partial t}\right|_{(x=c,y,z,t)}\mathrm{d}y\,\mathrm{d}z, \tag{4.13}$$

where

$$\left.\frac{\partial \omega_x}{\partial t}\right|_{(x=c,y,z,t)} = \omega_x\frac{\partial u}{\partial x} - \left(v\frac{\partial \omega_x}{\partial y} + w\frac{\partial \omega_x}{\partial z}\right) + \frac{2\pi}{Re}\left(\frac{\partial^2\omega_x}{\partial x^2} + \frac{\partial^2\omega_x}{\partial y^2} + \frac{\partial^2\omega_x}{\partial z^2}\right). \tag{4.14}$$

The first term on the right of (4.14) represents vortex stretching in the $\hat{x}$-direction, and it has no net contribution to (4.13). The total contributions by the second and third terms of (4.14) contain advective and diffusive effects, respectively.

The advective term includes flows due to all possible sources, which include the three advective effects of the vortex bridges on the threads, each thread on the other, and each thread on itself. The first advective effect contributes a mostly upwards flow (and the curvature reduction already discussed), the second effect contributes a mostly downwards flow, and the last effect contributes the self-induction flow due to curvature (at earlier times, these latter two increase the curvature through positive feedback). Since the first two contribute mostly in the vertical direction, we expect that the self-induction term is the major contributor to (4.13)‡. This belief is consistent with the time evolution of the advective contribution to (4.13) shown in figure 20(*b*). Note in particular that this contribution, for each *Re*, increases when κ increases, peaks at a time consistent with the time of peak κ, decreases thereafter when κ decreases, and is always negative (i.e. leads to a smaller y_c/smaller thread separation). Even though the curvature remains larger for larger *Re*, the advective contribution to y_c decreases more rapidly. We believe this is because the circulation of the threads decreases more rapidly for larger *Re*, and the magnitude of self-induction of a curved vortex tube is proportional to its circulation.

Now consider the diffusive term. This term is non-intuitive, as diffusion might be expected to be less important in general for larger *Re*. However, for our results, the integrated effect of this term contributes more significantly to (4.13) for larger *Re*. First, we note that the first part of the diffusive term contributes only a few percent of the total diffusive contribution (for the *Re* we have considered); however, we must leave open the possibility that this may not be true in cases of much larger κ (achieved for larger *Re* than we have considered). The contribution by the remainder of the diffusive term represents asymmetric diffusion of ω_x (with respect to the centroid) within plane c, and its time evolution is shown in figure 20(*b*). At early times (not shown), diffusion is nearly (radially) symmetric with respect to the thread centroid, and its contribution to (4.13) is nearly zero. However, its contribution to (4.13) is

---

† As for (4.3), in the stratified cases, the following area integrals are computed over only the region bounded by the zero vorticity line between the primary and background vorticity.

‡ Virk *et al.* (1995) discuss these advective contributions in greater detail; however, they do not retain the diffusive term, which appears to play an important role in our simulations.

always positive (i.e. leads to a larger y_c and a larger thread separation), and increases to some peak value, whereafter it decreases slowly in magnitude.

A simple physical interpretation of the diffusive term is that the deformation of the thread cross-section (see § 4.1 and in particular figures 9 and 10) and the proximity of the centroid to the centreplane results in more diffusion of vorticity away from the centreplane than towards it (relative to y_c); a more detailed interpretation and analysis may appear in future work. We note that, for each *Re*, the magnitude of the diffusive contribution increases as the deformation increases, and peaks at a time consistent with the time of peak deformation (judged visually). A larger *Re* first leads to less deformation (the thread core size grows more slowly), but then leads to both an earlier deformation (the thread nears the centreplane more rapidly due to both more rapid instability growth and more rapid curvature growth), and a more significant deformation (the limit on cross-diffusion is enhanced) of the thread cross-section (see figure 20*b*). Therefore, a larger *Re* results in a larger and more rapidly attained peak contribution by the diffusive term. We note that the time at which this peak is achieved is in each case consistent with the time at which $\Gamma_c/\Gamma_f = 1/2$, and that the diffusive contribution thereafter falls off more rapidly for larger *Re*. This observation may provide important guidance for revised reconnection models, as the 'singularity time' is often defined as the time at which the reconnection is 50% complete (e.g. § 4.3).

Once the diffusive contribution to (4.13) attains a larger magnitude than the advective contribution, this remains true for the remainder of our evolutions. Past this time, $\partial y_c/\partial t > 0$, and the thread separation increases. Even though curvature reduction (as explained by Melander & Hussain) does play a very important role, we therefore see the deformative/diffusive process as a second effect (similar to yet distinct from the curvature reversal of Melander & Hussain) which prevents complete reconnection. We further believe that the initial conditions and *Re* of a particular vortex reconnection experiment will determine the importance of the deformative/diffusive effect compared to the curvature reversal effect (and perhaps other yet undiscovered effects).

Now that we have discussed the completeness of reconnection issue for our unstratified flows in great detail, we discuss the completion of reconnection in our $Fr = 1$ and $Fr = 2$ flows (see § 4.2, and in particular figure 11) within the same context. As before, κ_z never changes sign in these flows, and so curvature reversal does not take place. To determine the role of the deformative/diffusive effect, we must strictly augment (4.14) with (4.5). Although the total contribution by this baroclinic term is negative during the time interval of interest, it is much smaller in magnitude than the contributions by the advective and diffusive terms. It is small in magnitude because, after $t \simeq 2$, the region of fluid carried with the vortices is internally well mixed (see figure 12 of this paper and figure 2 of Garten *et al.* 1998), and the area integral in (4.13) is computed over only the region of the primary vorticity. Its contribution is negative because it decreases ω_x mostly in the outer boundary region where $y - y_c > 0$.

Consider the contribution by the advective term. The initial instability grows more rapidly for smaller *Fr*, and subsequently the curvature of each thread grows more rapidly. The advective term now also includes the advective effect of the baroclinic vorticity on the thread (e.g. the evolution of $\langle b\rangle/b_0$ in figure 6), which also increases in importance for smaller *Fr*. Both of these effects contribute to the dramatic, more rapid increase in magnitude of the advective contribution for smaller *Fr* shown in figure 20(*d*). As for the unstratified cases, the advective contribution peaks and then decreases in magnitude due to both curvature reduction (via the flow induced by the vortex bridges) and a decrease in thread circulation. Since the reconnection proceeds more rapidly for smaller *Fr*, both of these effects lead to the more rapid decrease from the peak for smaller *Fr* also evident in figure 20(*d*).

In the unstratified case, this decrease led to a smaller magnitude contribution to (4.13) than by the diffusive term; however, this is not true for these stratified cases (see figure 20*d*). This is somewhat surprising, because the more rapid decrease in y_c (see figure 20*c*) should result ideally in greater deformation of the thread cross-section. Indeed, the contribution by the diffusive term does increase more rapidly for smaller *Fr* (see figure 20*d*). However, it does not increase rapidly enough to overtake the advective term, and it peaks (as in the unstratified case, at a time consistent with when $\Gamma_c/\Gamma_f = 1/2$), and then decreases without ever doing so. Therefore, $\partial y_c/\partial t$ never changes sign, the thread centroids advect towards the centreplane (i.e. y_c decreases) at all times (see figure 20*c*), and eventually cross-diffusion eliminates the thread entirely. We note that in the $Fr = 4$ and $Fr = 8$ cases (not shown), the diffusive term is robust enough to flip the sign of $\partial y_c/\partial t$, and the time evolution of b_c is nearly identical to the unstratified result.

5. The critical *Fr* separating the regimes of behaviour

The points we have discussed indicate clearly that there is some critical *Fr*, Fr_C, across which a dramatic, qualitative shift in the behaviour occurs. Enhanced Crow instability and subsequent more rapid reconnection results for *smaller Fr* within the range $Fr > Fr_C$, while suppressed Crow instability and little or no reconnection results for smaller *Fr* within the range $Fr < Fr_C$. Although many questions regarding this transition could be raised, we restrict our attention to the following points.

Our results suggest that the time evolution of $\langle b \rangle$ reveals the regime that a particular simulation is in, and we therefore consider its *Fr*-dependence to obtain an approximate value for Fr_C. Since we are convinced that the physical mechanisms responsible for a time-evolving $\langle b \rangle$ are two-dimensional, we have augmented our results with a number of two-dimensional simulations calculated with different *Fr*, *Re*, and *Pr*. (See Garten *et al.* 1998 for discussion of the two-dimensional numerical model.) Figure 21(*a*) shows the time evolution of the separation distance, *b*, of two-dimensional vortex pairs at different *Fr*, but all with $Re = 942$ and $Pr = 1$. Note that *b* increases for $Fr \leqslant 0.65$, and decreases for $Fr \geqslant 0.675$; we therefore believe that $0.65 < Fr_C < 0.675$.

We wish to estimate the dependence of Fr_C on *Re* and *Pr*. Therefore, we continue to use our two-dimensional conceptualization, and we consider again the underlying causes of an increase or decrease in *b*. In the large *Fr* limit ($Fr \to \infty$), the background is of nearly constant density, and the two-dimensional vortex pair would propagate without change until a viscous timescale were reached. So long as *Fr* is finite ($Fr > Fr_C$), however, previous (Garten *et al.* 1998) and current (not shown) results indicate that baroclinic vorticity forms due to the stratification, concentrates mostly on the outer sides of the primary vortices, and then advects the primary vortices towards one another (*b* decreases). These results have also shown that a decrease in *b* is discernible by $t \simeq 2$, independent of *Fr*. In the small *Fr* limit ($Fr \to 0$), the fluid equations are nearly linear, and perturbations may be described in terms of linear gravity waves which propagate away from the point of origin. Indeed, previous (Garten *et al.* 1998)†

---

† We note that figures 7 and 10 in Garten *et al.* (1998) were erroneously swapped in publication. In that paper, the $Fr = 1/8$ case is actually depicted in figure 10, and the $Fr = 1/4$ case is actually depicted in figure 7. We apologize for the potential confusion, but wish to warn the careful reader.

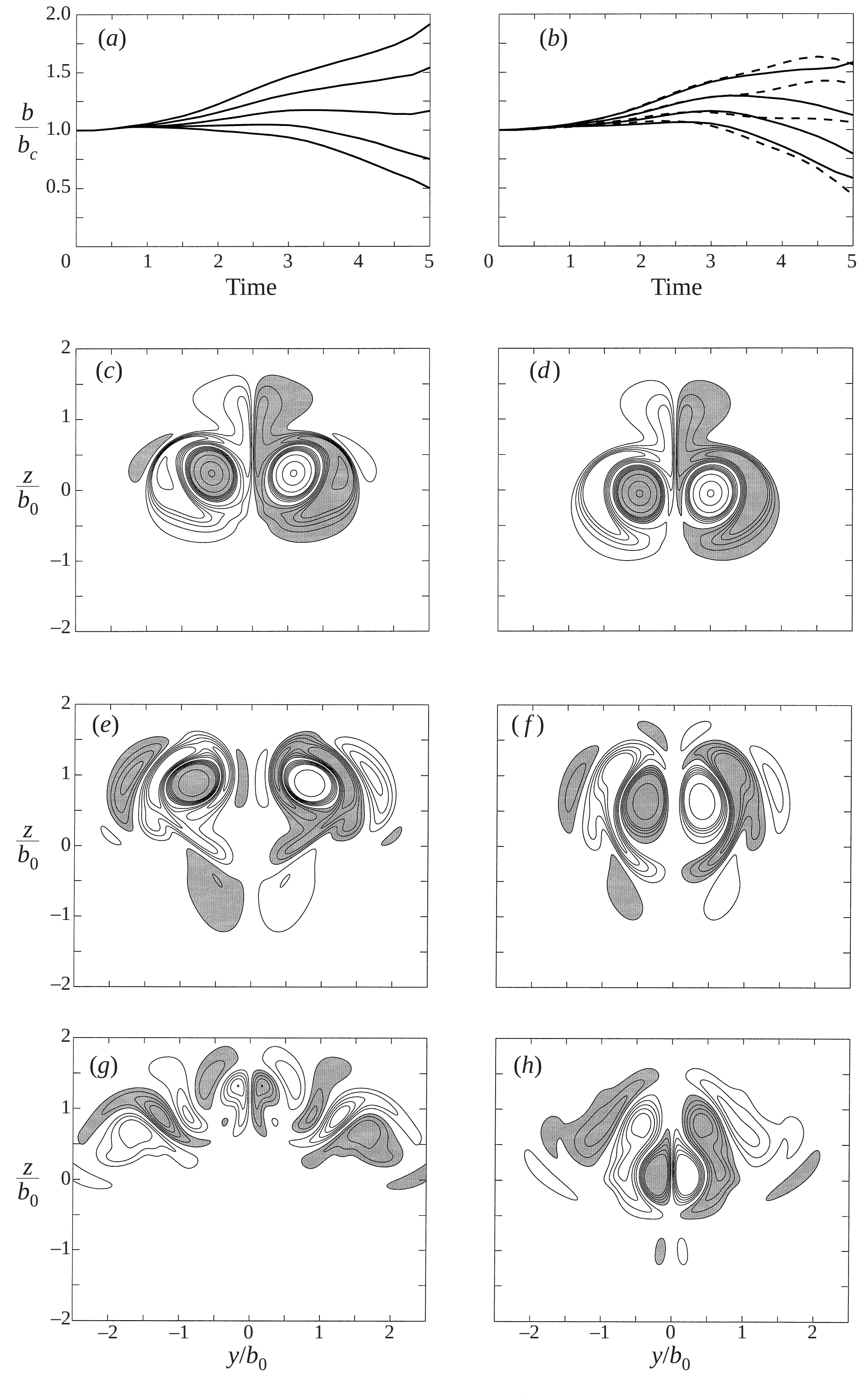

FIGURE 21. For caption see facing page.

and current (e.g. figure 21*g*) results indicate that these flows display the pattern of gravity wave radiation from a localized source within roughly 1–2 buoyancy periods ($T_B = 2\pi/N = 2\pi Fr$) after the initial vortex pair excitation. These results also show that, at earlier times, regions of baroclinic vorticity concentrate on the outer sides, in between, and all around each of the original vortices, with the net advective effect of driving the original vortices away from one another (b increases). This motion is discernible by $T_B/2$, and continues up to times at which the original vortices lose their identity within the increasingly complex flow field.

Note that for $Fr \simeq Fr_C$, $T_B/2 \approx 2$. Therefore, we expect the beginnings of an increase ($Fr < Fr_C$) or decrease ($Fr > Fr_C$) in b for $Fr \simeq Fr_C$ by $t \simeq 2$, an expectation borne out qualitatively by the observations in figure 21(*a*). So, we consider the vorticity field at $t = 2$ for two Fr on either side of Fr_C (see figure 21*c*, *d*). Even though the differences in the distribution of baroclinic vorticity are small at this time in the evolutions (their Fr are nearly equal), they nonetheless reveal which side of Fr_C each case lies on. Together with other solutions which we have examined (not shown), these results lead us to believe that the relevant issue is the amount of baroclinically produced vorticity that resides in between the primary vortices during this crucial early time. In the $Fr = 0.7$ (figure 19*d*) and all other $Fr > Fr_C$ cases we have examined, baroclinic vorticity is advected around each primary vortex and away from the region between them; later times in the flow (see figure 21*f*, *h*) look similar to the two-dimensional cross-sections shown in figures 12–14. In the $Fr = 0.6$ (figure 21*c*) and all other $Fr < Fr_C$ cases we have examined, baroclinic vorticity builds up in all regions surrounding the primary vortices, and the magnitude of these regions is greater everywhere; later times in the flow (see figure 21*e*, *g*) look similar to figure 7 in Garten *et al.* (1998). It is through understanding of this build up of baroclinic vorticity between the primary vortices (or lack thereof) that we hope to estimate the dependence of Fr_C on Re and Pr.

Consider whether or not the baroclinic source of vorticity can by itself explain directly the different behaviour in the two regimes. We find that, for $Fr \approx Fr_C$, the evolution of the (non-dimensional) density field is virtually identical up to at least $t = 1$. The density gradients are thus also nearly identical, and so the magnitude of the baroclinic source varies in comparison as $1/Fr^2$ (see e.g. (4.5)) at these early times in the evolution. Although the different amounts of baroclinic vorticity thus produced are clearly important to later times in the flows, they are not in themselves adequate to explain the different distributions of baroclinic vorticity we observe by $t \simeq 2$. This is because the advection of the baroclinic vorticity around each primary vortex should be largely independent of the magnitude of the baroclinic vorticity (presuming it is much less than the magnitude of the primary vortices). To expand slightly on this point, the advection of the baroclinic vorticity around each primary vortex should

FIGURE 21. (*a*) The time evolution of the separation distance of two-dimensional vortex pairs with $Re = 942$, $Pr = 1$, and, from top to bottom in the panel, $Fr = 0.6$, 0.625, 0.65, 0.675, and 0.7. (*b*) As in (*a*), but for $Re = 942$, $Pr = 7$, and $Fr = 0.65$,0.675,0.7, and 0.725 (solid lines) and $Re = 9420$, $Pr = 1$ and $Fr = 0.725$, 0.75, 0.775, and 0.8 (dashed lines). (*c–h*) Contours of vorticity for the two-dimensional cases with $Re = 942$, $Pr = 1$, and $Fr = 0.6$ (left) and 0.7 (right) at $t = 2$ (*c*, *d*), $t = 4$ (*e*, *f*), and $t = 6$ (*g*, *h*). Contour levels at $\pm 10, \pm 20, \pm 30$, etc. show the distribution of high-magnitude vorticity, while additional contour levels at $\pm 1, \pm 2, \pm 3, \pm 4, \pm 5$ illustrate the distribution of low-magnitude vorticity, and all regions enclosed by negative contours are shaded.

ideally be governed by an advective process given roughly by

$$\frac{\partial \omega_b}{\partial t} = -\boldsymbol{v}_p \cdot \nabla \omega_b, \tag{5.1}$$

where here $\boldsymbol{v}_p$ represents the rotational velocity due to each primary vortex and ω_b represents the distribution of baroclinic vorticity. Insofar as this view is accurate, the removal rate of baroclinic vorticity from the region between the vortices is proportional to the amount of baroclinic vorticity in that region. Therefore, a larger-magnitude baroclinic source does not lead directly to a buildup of baroclinic vorticity between the primary vortices.

The key insight is that the *effective* rotational/removal velocity magnitude can be *reduced* significantly from $|\boldsymbol{v}_p|$ by the advective effects of the baroclinic vorticity itself. The larger the amount of baroclinic vorticity, the larger the reduction in $|\boldsymbol{v}_p|$, and the greater the potential for baroclinic vorticity to build up in the area between the primary vortices (leading to a further reduction in $|\boldsymbol{v}_p|$, and so on). We believe that for $Fr < Fr_C$, this process successfully prevents the removal of baroclinic vorticity from the region between the vortices, and the evolution then diverges rapidly from the $Fr > Fr_C$ case.

Note that neither *Re* nor *Pr* appear explicitly in any of our arguments. However, the distribution of density gradients at early times is part of our reasoning, and the rate at which these gradients diffuse is affected by *Re* and *Pr* (e.g. (2.7)). Larger *Re* and/or *Pr* allow density gradients to remain larger, and so the baroclinic source is effectively increased in magnitude (for fixed *Fr*). Therefore, we expect Fr_C to shift to larger values for increasing *Re* and/or *Pr*. Figure 19(*b*) shows the time evolution of *b* for two-dimensional vortex pairs with different *Fr*, *Re*, and *Pr*, and appears to support our belief within the portion of parameter space we have considered. Specifically, $Fr_C \approx 0.675$ for $Re = 942$ and $Pr = 7$, while $Fr_C \approx 0.775$ for $Re = 9420$ and $Pr = 1$.

We see no reason why Fr_C should be significantly different for the three-dimensional case. However, the computational cost to make this determination is too great at present, and so we must leave open the possibility that the detailed dynamics of the three-dimensional distribution of vorticity could alter Fr_C by some small amount. We do note that, since the separation distance is not constant along the vortex tubes, the closest portions of the vortex tubes could evolve at an effective $Fr > Fr_C$ while their remainder evolve at an effective $Fr < Fr_C$ (for constant circulation, $Fr \sim 1/b^2$). We believe this could result in a vortex ring that forms very quickly from the original vortex tubes, but loses its dominance of the flow with the rapid advent of baroclinic vorticity.

6. Discussion

We have found that ambient stratification can affect substantially the evolution of anti-parallel vortex pairs which undergo the Crow instability and subsequent vortex reconnection. Our unstratified simulations show that the growth rate of the Crow instability has some *Re* dependence in the range of *Re* we are able to access, and we have presented a simple extension to Crow's model to explain this dependence. Our stratified simulations show that relatively strong ambient stratification ($Fr \leqslant 2$) further alters the growth of the Crow instability when baroclinically produced vorticity either advects the primary vortices towards one another ($Fr > Fr_c$), leading to a faster growth, or away from one another ($Fr < Fr_c$), retarding the growth and preventing significant vortex reconnection from ever commencing. For the latter regime, the growth of the three-dimensional instability is sufficiently slowed that a two-dimensional description becomes increasingly sufficient for smaller Fr (see Jaderberg 1980; Garten 1997; and Garten *et al.* 1998 for studies of two-dimensional vortex pairs in strong ambient stratification). We also found that the boundary for these different regimes of behaviour lies at $Fr_C \approx 2/3$ for $Re = 942$ and $Pr = 1$, and that Fr_C increases slightly for larger Re and/or Pr.

Our unstratified simulations also elucidate the Re dependence of the vortex reconnection process. Although a larger Re delays the commencement of the vortex reconnection, it increases the rate at which the vortex reconnection proceeds once it does commence, and increases the asymptotic fraction of reconnected circulation (i.e. $\Gamma_r/\Gamma_f(t \rightarrow \infty)$). We defined a reconnection timescale, t_R, as the negative inverse of $\mathrm{d}\Gamma_c/\mathrm{d}t$ at the instant in time when $\Gamma_c = \Gamma_f/2$, and we found that $t_R \sim 1/Re$, in agreement with the extension of Shelley *et al.* (1993) to the work of Siggia & Pumir (1987). We then discussed a deformative/diffusive effect which prevents the attainment of complete reconnection. Although curvature *reduction* plays an important role in this process, our discussion indicates that it should be viewed as different from the curvature *reversal* effect discussed by Melander & Hussain (1989).

Our stratified simulations also show that the vortex reconnection phase of the evolution is accelerated in moderate to strong ambient stratification ($1 \leqslant Fr \leqslant 8$). The advection by the baroclinic vorticity that accelerates the Crow instability (for a smaller range of Fr) later increases the vorticity gradients at the centreplane and thereby enhances the cross-diffusion that results in vortex reconnection. For our $Fr = 1$ and 2 cases, the continuous advection by the baroclinic vorticity leads to the complete elimination of the threads, while for the larger Fr cases, threads continue to survive up to very late times (past the times at which simulations were discontinued). For our fixed Re, we have found that ambient stratification decreases t_R by an amount roughly proportional to $1/Fr$, in qualitative agreement with our extension to the previous model.

It is interesting to speculate on the relevance of our single-wavelength, small-Re, laminar solutions for predictions on how the Crow instability and subsequent vortex reconnection proceed in large-Re, turbulent flows. One truly naive approach would be to assume that random motions and mixing brought on by ambient turbulence are in some sense equivalent to an eddy viscosity that decreases the *effective* Re of the flow. Insofar as this concept is valid, our results could be very relevant. However, we are quite open to the idea of ambient turbulence nurturing other instabilities that disrupt the evolution and alter it significantly from what occurs in the cases we have considered. We have computed simulations with additional wavelengths (larger than the vortex spacing) perturbed in both symmetric and antisymmetric configurations, but our Re is apparently too small for the evolution to alter significantly. This is particularly disappointing given the experimental results ($Re = 2750$) of Leweke & Williamson (1998), who show that simultaneous modulated growth of short waves (in their case, of the same order as the vortex core size), and their subsequent breakdown, inhibit formation of distinct vortex rings, and lead to distinct periodic regions of turbulent motion. The effects of these short waves on the reconnection process itself are not clear to us at present, and simulations to explore this situation may become the focus of future research. Although our results thus yield little insight on how ambient turbulence might disrupt the evolution, a planned analysis of three-dimensional vortex pairs evolving in ambient shear layers may provide additional clues.

We have benefited from discussions with Philippe Spalart of Boeing Aircraft, Bob Robins of NorthWest Research Associates, Fazle Hussain of the University of Houston, and Øeyvind Andreassen of the Norwegian Defense Research Establishment, as well as excellent feedback from an anonymous referee. We are also grateful to Per Øyvind Hvidsten of the Norwegian Defense Research Establishment for assistance in preparing the volume renderings used in the paper. This work was supported by the Air Force Office of Scientific Research under grant F49620-98-C-0029 and the National Science Foundation under grants ATM-9618004 and ATM-9708633. Computational resources were provided by the Pittsburgh Supercomputing Center under grant ATM96004P, and by NPACI at the San Diego Supercomputing Center and the University of Texas under grant MCA98N008.

REFERENCES

Andreassen, Ø., Wasberg, C. E., Fritts, D. C. & Isler, J. R. 1994 Gravity wave breaking in two and three dimensions, I. Model description and comparison of two-dimensional evolutions. *J. Geophys. Res.* **99**, 8095.

Aref, H. & Zawadzki. I. 1991 Linking of vortex rings. *Nature* **354**, 50.

Ashurst, W. T. & Meiron, D. 1987 Numerical study of vortex reconnection. *Phys. Rev. Lett.* **58**, 1632.

Boratav, O. N., Pelz, R. B. & Zabusky, N. J. 1992 Reconnection in orthogonally interacting vortex tubes: direct numerical simulations and quantifications. *Phys. Fluids* A **4**, 581.

Buntine, J. D. & Pullin, D. I. 1989 Merger and cancellation of strained vortices. *J. Fluid Mech.* **205**, 263.

Canuto, C., Hussaini, M. Y., Quarteroni, A. & Zang, T. A. 1988 *Spectral Methods in Fluid Dynamics.* Springer.

Corjon, A., Risso, F., Stoessel, A. & Poinsot, T. 1996 Three-dimensional direct numerical simulations of wake vortices: atmospheric turbulence effects and rebound with crosswind. In *The Characterization and Modification of Wakes from Lifting Vehicles in Fluids*, AGARD-CP-584, p. 28–1. AGARD Publications.

Crow, S. C. 1970 Stability theory for a pair of trailing vortices. *AIAA J.* **8**, 2172.

Crow, S. C. 1974 Motion of a vortex pair in a stably-stratified fluid. *Poseidon Res. Rep.* No. 1.

Crow, S. C. & Bate, E. R. 1976 Lifespan of trailing vortices in a turbulent atmosphere. *J. Aircraft* **13**, 476.

Fohl, T. & Turner, J. S. 1975 Colliding vortex rings. *Phys. Fluids* **18**, 433.

Garten, J. F. 1997 An investigation of the effects of environmental stratification and shear on the evolution of vertically-propagating vortex pairs. Doctoral Dissertation, University of Colorado.

Garten, J. F., Arendt, S., Fritts, D. C. & Werne, J. 1998 Dynamics of counter-rotating vortex pairs in stratified and sheared environments. *J. Fluid Mech.* **361**, 189.

Greene, G. C. 1986 An approximate model of vortex decay in the atmosphere. *J. Aircraft* **23**, 566.

Hussain, F. 1986 Coherent structures and turbulence. *J. Fluid Mech.* **173**, 303.

Jaderberg, L. K. 1980 A method for computing the internal wave field around a nonlinear stratified flow. Doctoral Dissertation, UCLA.

Jeong, J. & Hussain, F. 1995 On the identification of a vortex. *J. Fluid Mech.* **285**, 69.

Kambe, T. 1983 A class of exact solutions of two-dimensional viscous flow. *J. Phys. Soc. Japan* **52**, 834.

Kerr, R. M. & Hussain, F. 1989 Simulation of vortex reconnection. *Physica* D **37**, 474.

Kida, S. & Takaoka, M. 1994 Vortex reconnection. *Ann. Rev. Fluid Mech.* **26**, 169.

Kida, S., Takaoka, M. & Hussain, F. 1989 Reconnection of two vortex rings. *Phys. Fluids* A **1**, 630.

Kida, S., Takaoka, M. & Hussain, F. 1991*a* Collision of two vortex rings. *J. Fluid Mech.* **230**, 583.

Kida, S., Takaoka, M. & Hussain, F. 1991*b* Formation of head-tail structure in a two-dimensional uniform straining flow. *Phys. Fluids* A **3**, 2688.

Kolmogorov, A. N. 1941 *Acad. Sci. USSR* **30**, 301.

Leweke, T. & Williamson, C. H. K. 1998 Cooperative elliptic instability of a vortex pair. *J. Fluid Mech.* **360**, 85.

Lissaman, P. B. S., Crow, S. C., MacCready, P. B., Tombach, I. H. & Bate, E. R. 1973 Aircraft vortex wake descent and decay under real atmospheric effects. *Transportation Systems Center R.* FAA-RD-73-120.

Melander, M. V. & Hussain, F. 1989 Cross-linking of two antiparallel vortex tubes. *Phys. Fluids* A **1**, 633.

Moore, D. W. 1972 Finite amplitude waves on aircraft trailing vortices. *Aero. Q.* **19**, 307.

Olsen, J. H., Goldburg, A. & Rogers, M. (Eds.) 1971 Aircraft wake turbulence and its detection. *Proc. Symp. on Aircraft Wake Turbulence, Seattle.* Plenum.

Oshima, Y. & Izutsu, N. 1988 Cross-linking of two vortex rings. *Phys. Fluids* **31**, 2401.

Pumir, A. & Kerr, R. M. 1987 Numerical simulation of interacting vortex tubes. *Phys. Rev. Letters* **58**, 1636.

Robins, R. E. & Delisi, D. P. 1996 Three-dimensional calculations showing the effects of stratification on the evolution of trailing vortices. In *Computation of Three-Dimensional Complex Flows.* Notes on Numerical Fluid Mechanics, vol. 53 (ed. P. Deville *et al.*) Vieweg, Braunschweig.

Robins, R. E. & Delisi, D. P. 1997 Numerical simulations of three-dimensional trailing vortex evolution. *AIAA J.* **35**, 1552.

Rogers, M. M. & Moin, P. 1987 The structure of the vorticity field in homogeneous turbulent flows. *J. Fluid Mech.* **176**, 33.

Saffman, P. G. 1990 A model of vortex reconnection. *J. Fluid Mech.* **212**, 395.

Saffman, P. G. 1992 *Vortex Dynamics.* Cambridge University Press.

Sarpkaya, T. 1983 Trailing vortices in homogeneous and density-stratified media. *J. Fluid Mech.* **136**, 85.

Schilling, V., Siano, S. & Etling, D. 1996 Dispersion of aircraft emissions due to wake vortices in stratified shear flows: A two-dimensional numerical study. *J. Geophys. Res.* **101**, 20965.

Scorer, R. S. & Davenport, L. J. 1970 Contrails and aircraft downwash. *J. Fluid Mech.* **43**, 451.

Shelley, M. J., Meiron, D. I. & Orszag, S. A. 1993 Dynamical aspects of vortex reconnection of perturbed anti-parallel vortex tubes. *J. Fluid Mech.* **246**, 613.

Siggia, E. D. & Pumir, A. 1987 Vortex dynamics and the existence of solutions to the Navier–Stokes equations. *Phys. Fluids* **30**, 1606.

Spalart, P. R. 1996 On the motion of laminar wing wakes in a stratified fluid. *J. Fluid Mech.* **327**, 139.

Spalart, P. R. 1998 Airplane trailing vortices. *Ann. Rev. Fluid Mech.* **30**, 107.

Spalart, P. R., Moser, R. D. & Rogers, M. M. 1991 Spectral methods for the Navier–Stokes equations with one infinite and two periodic directions. *J. Comput. Phys.* **96**, 297.

Tomassian, J. D. 1979 The motion of a vortex pair in a stratified medium. Doctoral Dissertation, UCLA.

Virk, D., Hussain, F. & Kerr, R. M. 1995 Compressible vortex reconnection. *J. Fluid Mech.* **304**, 47.